

# Spatial organization of a chemoreceptor guanylate cyclase in the flagellum of *Arbacia punctulata* sperm

Inaugural-Dissertation

zur

Erlangung des Doktorgrades

der Mathematisch-Naturwissenschaftlichen Fakultät

der Universität zu Köln



vorgelegt von

Domenica Farci

aus Cagliari, Italia

Köln

2017

Berichterstatter: Prof. Dr. U. B. Kaupp

Prof. Dr. G. Schwarz

Tag der mündlichen Prüfung: 04/10/2017

## Table of contents

<b>Summary</b> .....	I
<b>Zusammenfassung</b> .....	II
<b>Abbreviations</b> .....	IV
<b>1. Introduction</b> _____	<b>1</b>
1.1 General outline of chemotaxis.....	1
1.2 Sperm chemotaxis .....	3
<i>Overview</i> .....	3
<i>Chemoattractant</i> .....	4
<i>Swimming behaviour</i> .....	6
<i>Signaling pathway in A. punctulata sperm</i> .....	8
<i>The importance of Ca<sup>2+</sup></i> .....	10
1.3 The family of guanylate cyclase receptors.....	12
<i>Overview</i> .....	12
<i>Ligand affinity and GC density in A. punctulata sperm</i> .....	15
<i>Supramolecular organization of receptors in sensory systems</i> .....	17
1.4 Aim .....	19
<b>2. Materials and Methods</b> _____	<b>20</b>
2.1 Materials .....	20
2.2 Sample preparation .....	20

2.3 Sample preparation for electron microscopy .....	21
2.4 Cryo-electron tomography .....	22
<i>Data acquisition by SerialEM</i> .....	23
2.5 Alignment and 3D reconstruction of tomograms .....	25
2.6 Sub-tomogram averaging .....	25
2.7 Statistics .....	27
<b>3. Results</b> .....	<b>29</b>
3.1 Cryo-electron tomography of the intact flagellum .....	29
3.2 The GC is organized as a helix that coils around the flagellum .....	39
3.3 The GC forms dimers .....	42
3.4 Structural parameters of GC dimers in a helix .....	49
<b>4. Discussion</b> .....	<b>51</b>
<i>Subsection 1 - Drawbacks and advantages of cryo-electron tomography</i> .....	51
<i>The problem of a low signal-to-noise ratio</i> .....	53
<i>Limits on the specimen thickness</i> .....	55
<i>The missing-wedge problem</i> .....	56
<i>The analysis of the supramolecular GC architecture avoiding the         missing-wedge effect</i> .....	59
<i>Subsection 2 - Biological insights from the GC density and its supramolecular     architecture</i> .....	61
<i>Density of the GC in the intact sperm flagellum</i> .....	61

<i>Distribution of GC along the flagellum.....</i>	62
<i>What might be the functional significance of the high density and uniform distribution of GC?.....</i>	63
<i>Higher-order organization of GC: a comparison with rhodopsin architecture and bacterial receptor array.....</i>	65
<i>Oligomeric state of GC.....</i>	67
<b>Literature .....</b>	<b>69</b>
<b>Acknowledgments .....</b>	<b>94</b>

## Summary

The sea urchin *Arbacia punctulata* is a model organism to study sperm chemotaxis and fertilization. A milestone in this research field was the discovery of the chemoreceptor guanylate cyclase (GC) that is situated in the plasma membrane of sperm flagella. GC binds a chemoattractant called *resact*, that is released by the oocyte of sea urchins. The sensitivity of *A. punctulata* sperm toward *resact* is so remarkably high, that they can follow a picomolar gradient of *resact* toward the egg. Even binding of single molecules can alter the swimming behavior of sperm.

Receptor-type guanylate cyclases serve as chemoreceptors in many species, but their oligomeric state and spatial organisation *in situ* are up to now unknown. In case of *A. punctulata* sperm, the GC is expressed in high copy numbers in the flagellar membrane. This high density allows probing its supramolecular architecture by cryo-electron tomography of frozen cells. Here I reveal the spatial organization of GC along the sperm flagellum, determining for the first time also its oligomeric state.

The GC is organized as a stripe of dimers, that winds like a helix around the flagellum. The chemoreceptors cover about 26% of the flagellar surface. The GC organization combined with the extremely high density and additional high affinity for *resact* may contribute to the exquisite chemotactic sensitivity of *A. punctulata* sperm. Finally, the helical organization might be a tool to contribute to the flexibility of the flagellum during beating.

## Zusammenfassung

Der Seeigel *Arbacia punctulata* ist ein Modellorganismus um Spermienchemotaxis und die Befruchtung der Eizelle zu untersuchen. Ein Meilenstein für das Verständnis Spermienchemotaxis war die Entdeckung eines Chemorezeptors, der Guanylat Zyklastase (GC), der in der Flagellenmembran der Spermien zu finden ist. Die GC bindet den chemischen Lockstoff *Resact*, der von der Eizelle ins Meerwasser abgegeben wird. Die Sensitivität der Spermien gegenüber *Resact* ist so hoch, dass sie einem Gradienten von picomolarer *Resact* Konzentration zur Eizelle folgen können. Schon die Bindung einzelner *Resact* Moleküle reicht aus, um die Schwimmbewegung der Spermien zu verändern.

Rezeptor-typ Guanylat Zyklastasen sind in vielen Spezies als Chemorezeptoren bekannt. Ihren oligomeren Zustand oder ihre räumliche Organisation im nativen Organismus hat bisher allerdings noch niemand aufgeklärt. In den *A. punctulata* Seeigelspermien ermöglicht eine extrem hohe GC Dichte die strukturelle Untersuchung mittels Kryoelektronentomografie. Ich konnte den Oligomeren Zustand und die Verteilung der GC auf dem Flagellum aufklären.

Die GC bildet eine Kette von Dimeren, die helikal um das Flagellum gewunden ist. 26% der Flagellenoberfläche werden von der GC bedeckt. Diese hohe Dichte, die räumliche Organisation sowie eine sehr hohe Affinität für *Resact* könnten einen Teil des Mechanismus bilden, der für die exquisite Sensitivität gegenüber *Resact* verantwortlich ist.

Die helikale Organisation könnte auch eine Struktur darstellen, die die Flexibilität des Flagellums während der Schwimmbewegung unterstützt.

## Abbreviations

°C	grad Celsius
[Ca <sup>2+</sup> ] <sub>i</sub>	intracellular Ca <sup>2+</sup> concentration
μL	micro liter
μm	micro meter
2D	2-dimensional
3D	3-dimensional
Å	angstrom
ASW	artificial sea water
ATP	adenosine 5''-triphosphate
ca.	circa
Ca <sup>2+</sup>	divalent calcium ion
CatSper	sperm-specific Ca <sup>2+</sup> channel
Ca <sub>v</sub>	voltage-gated Ca <sup>2+</sup> channels
CCC	cross-correlation coefficient
CCD	charge-coupled device
CD	cyclase domain
CEMOVIS	cryo-electron microscopy of vitreous sections
cGMP	3''5''-cyclic guanosine monophosphate
CNG	cyclic nucleotide-gated
CNGK	cyclic nucleotide-gated K <sup>+</sup> channel

CO	carbon monoxide
CTF	contrast transfer function
Da	Dalton (1,6601x10 <sup>-27</sup> kg)
DD	dimerisation domain
e <sup>-</sup>	electron
e.g.	exempli gratia – for example
ECD	extracellular domain
EM	electron microscopy
ET	electron tomography
et al.	et alii or et aliae
eV	electron Volt
fM	femto molar
FSC	Fourier Shell Correlation
GC	guanylate cyclase
GDP	guanosine diphosphate
GMP	guanosine monophosphate
GPCR	G protein-coupled receptor
GTP	guanosine-5''-triphosphate
h	hours
HCN	hyperpolarization-activated and cyclic nucleotide-gated
i.e.	channel
ICD	id est – that is

k	intracellular domain
K <sup>+</sup>	kilo
kDa	monovalent potassium ion
keV	kilo Dalton
KHD	kilo electron volt
kV	kinase-homology domain
L	kilo volt
m	liter
m	meter
M	milli
min	molar
mL	minutes
mm	milli liter
mM	milli meter
mV	milli molar
Mw	milli Volt
Na <sup>+</sup>	molecular weight
sNHE	monovalent sodium ion
nm	voltage-gated sperm-specific sodium/proton exchanger
nmol	nano meter
NO	nano Mol
p	nitrogen monoxide

PDE	pico
pH	phosphodiesterase
pm	activity of hydrogen ions
pM	pico meter
s	pico molar
SNR	second
TEM	signal-to-noise ratio
TM	transmission-electron microscopy
V	transmembrane domain
v/v	volt
X-ray	volume/volume
$\alpha$	energetic high-frequency electromagnetic radiation
$\mu$	alpha
	micro

# 1. Introduction

## 1.1 General outline of chemotaxis

Composed of the Greek words χημεία = chemical, and τάξις = arrangement, the term chemotaxis indicates the directed movement of an organism (single cell or multicellular) in response to a chemical stimulus present in the environment (Hugh 1911). In an ever-changing environment, chemotaxis is essential to sense these changes and respond accordingly. Chemotaxis is ubiquitous across phyla (from bacteria to eukaryotes) and serves different functions. Bacteria use chemotaxis for basic survival strategies as swimming toward food molecules or avoiding poisonous chemicals (e.g. glucose or phenol, respectively) (Hazelbauer 1988; Armitage 1992a; Armitage 1992b). Eukaryotes use chemotaxis for fertilization (swimming of sperm towards the egg) (Kaupp and Alvarez 2016; Wachten *et al.* 2017; Kaupp and Strünker 2017), tissue growth (embryogenesis, angiogenesis, migration of neurons – Wiseman *et al.* 1988; Gundersen 1985; Swaney *et al.* 2010; Kilic *et al.* 2016; Murray 2017), and immune responses (migration of lymphocytes and macrophages – Burnett *et al.* 2017; Romanova *et al.* 2017) – to list a few functions.

Important steps for understanding the mechanisms underlying chemotaxis are the identification of (1) the chemical compound (chemoattractant) that initiates the motility response, (2) the chemoreceptor that “senses” the chemoattractant, (3) the signaling pathway allowing the cell to process and respond to the stimulus, and finally (4) the motor or steering response itself. Cells or microorganisms probe a chemical

gradient by two different mechanisms: spatial or temporal sampling of the chemoattractant. Spatial sensing refers to a mechanism to detect a chemoattractant gradient by comparing signals received by sensor regions which are independent and spatially separated on the cell surface (Dusenbery 1992, Dusenbery 1998). This mechanism allows determining the direction of a gradient across the cell extension. By contrast, temporal sampling refers to a mechanism by which a cell moving in a chemoattractant field gains information about the direction of the gradient by integrating the chemical signals perceived over time along its swimming path (temporal changes of the chemoattractant concentration - Dusenbery 1992, Dusenbery 1998). Usually, small and rapidly moving cells use temporal sampling (e.g. bacteria - Swaney *et al.* 2010; Berg and Brown 1972), whereas large and slowly moving cells use spatial sensing (e.g. amoebae or immune cells - Iglesias 2012). The reason behind this difference is given by Berg and Purcell (1977): the precision of concentration measurements increases with the square root of the number of bound molecules  $n$  or the difference  $\Delta n = n_1 - n_2$ ; that is, the number of molecules detected at different time points or at difference sites on the cell surface.  $\Delta n$  during temporal sampling is larger for fast cells compared to slow ones, because the gradient is measured across a longer distance. Similarly, in large cells, receptor regions are widely separated and, therefore,  $\Delta n$  is larger. Considering these general rules, it is not obvious, which sensing mechanism is best for sperm: sperm are large compared with bacteria (the length of the flagellum is 45  $\mu\text{m}$  versus 5  $\mu\text{m}$  of a bacterial cell), but move about 2,000-fold faster compared with amoebae (180  $\mu\text{m s}^{-1}$  versus 0.1  $\mu\text{m s}^{-1}$ ). Previous reports provided some evidence that sperm use a temporal sensing mechanism (Strünker *et al.*

2006): the cyclic nucleotide-gated K<sup>+</sup> (CNGK) channels are distributed along the entire length of the flagellum (Bönigk *et al.* 2009), and hyperpolarization is expected to passively spread within a few milliseconds along the flagellum (see Hille (2001) for basics of electrical signaling). Because hyperpolarization evokes a Ca<sup>2+</sup> response that controls navigation, it is expected that the Ca<sup>2+</sup> influx occurs along the entire flagellum (see discussion for more details). Accordingly, spatial sampling is not needed or unlikely to occur. More recently, a caged chemoattractant was used to precisely measure the spatio-temporal delivery of a stimulus pattern showing that sea urchin sperm use temporal sensing to translate a spatial concentration pattern into a temporal pattern of Ca<sup>2+</sup> oscillations and steering response (Kashikar *et al.* 2012). Finally, the sampling time is inversely related to the stimulus: with increasing chemoattractant concentrations, the sampling time shortens (Alvarez *et al.* 2012; Kashikar *et al.* 2012). This observation might also hint to a temporal sampling mechanism and can be considered as a kind of kinetic adaptation to high stimulus levels.

## **1.2 Sperm chemotaxis**

*Overview.* Sperm from mammals and invertebrates use various sensing mechanisms to capture physical or chemical cues to find the egg. In mammals, three different sensory mechanisms have been suggested to guide sperm through the oviduct: chemotaxis (Kaupp *et al.* 2008), rheotaxis (Miki and Clapham 2013), and thermotaxis (Bahat *et al.* 2003). Due to the difficulties to emulate the native conditions that mammalian

sperm encounter during fertilization (e.g. temperature gradient, large changes in ions concentrations, interaction with the epithelial layer of the oviduct – Suarez and Pacey 2006; Knobil and Neill 2015), none of these three proposed mechanisms is well understood. By contrast, marine invertebrates release their gametes into the water, where sperm can swim freely. In this case, the native environment can be emulated in the laboratory and the 2D and 3D swimming of sperm can be studied with reasonable precision (Böhmer *et al.* 2005; Corkidi *et al.* 2008; Jikeli *et al.* 2015). It is now well established that sperm from many marine invertebrates use chemotaxis to locate the egg.

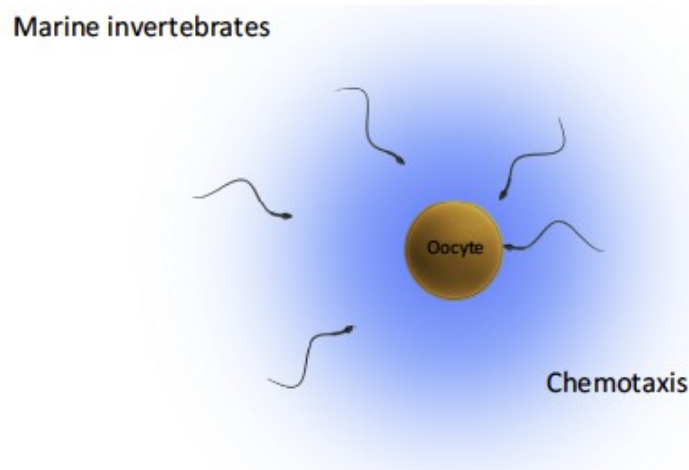


**Figure 1.** Chemotaxis for sperm in marine invertebrates. Chemotaxis refers to the directed movement of cells in a gradient of a chemical substance also called the chemoattractant. It is based on chemosensation. (Kaupp and Strünker 2017).

*Chemoattractant.* To overcome challenges to reach and fertilize the egg, sperm from different species have developed their unique signaling molecules and mechanism (for

review see Wachten *et al.* 2017; Kaupp and Strünker 2017). Sperm from different species respond to a species-specific chemoattractant (Olson *et al.* 2001; Rifell *et al.* 2002; Kaupp *et al.* 2003; Kilic *et al.* 2009; Burnett *et al.* 2011). In mammals, sperm might be instructed by long- and short-range cues to navigate by chemotaxis, rheotaxis, thermotaxis, or a combination of them (Alvarez *et al.* 2014). Although numerous molecules - from odorants to gases - have been proposed to attract mammalian sperm, their function as chemoattractant has not been as clearly established as for chemoattractants of sperm from marine invertebrates. Quite generally, as chemotaxis for mammalian sperm is debated, reports on mammalian chemoattractants should be taken with a grain of salt.

A notable and established example of sperm chemotaxis comes from the sea urchin *Arbacia punctulata* (Kaupp and Alvarez 2016; Wachten *et al.* 2017), for which the chemoattractant, chemoreceptor, signaling pathway, and swimming behaviour have been firmly established. In *A. punctulata*, a small peptide of 14 amino-acid residues called *resact* was isolated from the egg jelly (Hansbrough and Garbers 1981), and the chemotactic response of *Arbacia* sperm to *resact* was firmly identified (Suzuki and Garbers 1984; Suzuki *et al.* 1984; Ward *et al.* 1985). The binding of *resact* is transduced into a behavioural swimming response in the tiny compartment of the flagellum, which serves as sensory antenna, propeller, and rudder.

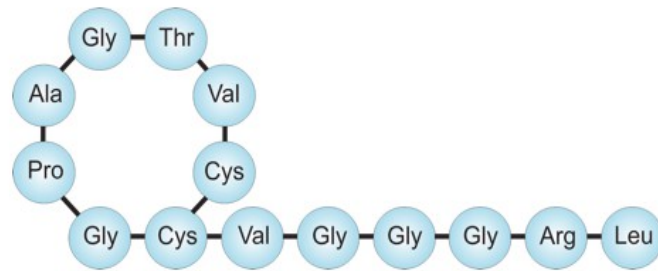


**Figure 2.** Resact molecule. Sequence of the chemoattractant resact.

*Swimming behaviour.* Thanks to the ability to emulate native conditions in the laboratory, sperm from marine invertebrates have been chosen as model to study and understand chemotaxis. Sperm and eggs are released into the seawater. To guide sperm navigation and enhance the probability of successful fertilization, eggs release the chemoattractant and, thereby, establish a chemical gradient (Kashikar *et al.* 2012; Kaupp and Alvarez 2016). Sperm sample single chemoattractant molecules impinging on their flagella and, performing several computational operations, integrate these binding events to generate a cellular and behavioural response (Kashikar *et al.* 2012; Alvarez *et al.* 2014; Pichlo *et al.* 2014). Sperm navigation has primarily been studied in two dimensions (2D): in shallow observation chambers, sperm are attracted to the glass/water interface by hydrodynamic forces (Elgeti *et al.* 2010; Elgeti and Gompper 2016), which facilitates observing cell movement in the focal plane (Böhmer *et al.* 2005). Although studies of 2D motility provided insights into chemotaxis, in the sea, sperm swim freely in three dimensions (3D). Using digital inline high-speed holographic microscopy, it has been possible to track sperm swimming unrestricted and to unveil the 3D navigation strategy (Jikeli *et al.* 2015). In a 2D gradient, sperm

swim on drifting circles, whereas in a 3D gradient, sperm swim on a helical path; during chemotactic steering, the swimming helix bends to align with the resact gradient (Jikeli *et al.* 2015). Furthermore, stimulus oscillations that result from the periodic component of helical swimming are translated into oscillatory motor responses that align the helix axis in a deterministic fashion. Finally, while swimming up the gradient, sperm adjust their course smoothly (helix bending, *on* response), whereas swimming down the gradient results in abrupt chemotactic turns (*off* response). These *on* and *off* responses can be attributed to characteristic biochemical and electrical signaling events in the flagellum (Jikeli *et al.* 2015; Kaupp and Alvarez 2016).

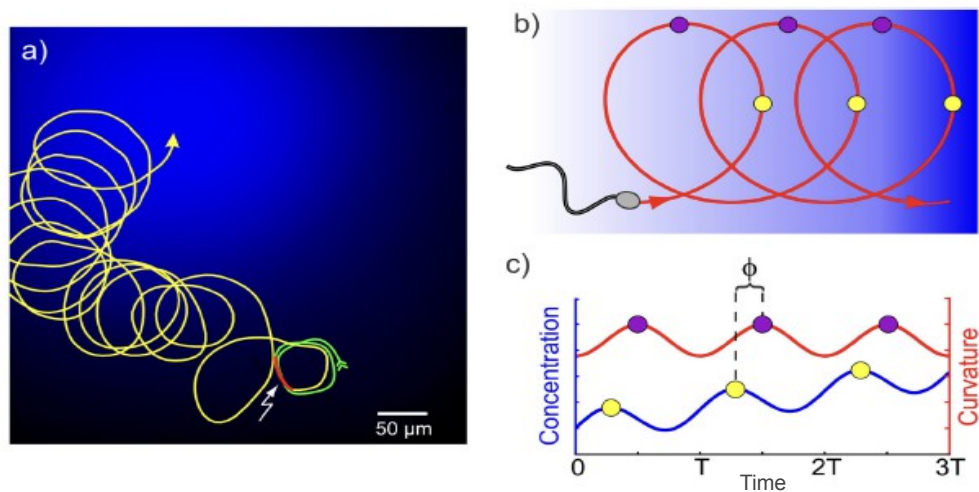


**Figure 3.** (a) Swimming path of sea urchin sperm in a chemoattractant gradient. Before stimulation, sperm swim on circles (green) at the glass/water interface of a shallow observation chamber. Upon release of the chemoattractant from its caged derivative (profile of the UV light shown in blue shades), the path curvature begins oscillating and sperm swim on drifting circles up the chemical gradient (yellow). The photolysis duration is shown in red. (b) Diagram of a sperm cell navigating in a

gradient of resact (blue). While swimming along a circular path, the cell is exposed to a concentration stimulus that varies periodically with the frequency of circular swimming. The local maximum is indicated by yellow dots. (c) The periodic modulation of the stimulus concentration (blue trace) encodes the spatial information about the chemical gradient. A chemotactic signalling pathway in the sperm flagellum transduces the periodic stimulus into a periodic steering response that regulates the swimming path curvature. Generically, a periodic concentration input (blue trace) produces a periodic modulation output of the path curvature (red trace). The phase difference  $\phi$  between the local maxima of the concentration (yellow dots on blue trace) and the local maxima of the path curvature (purple dots on red trace) determines the direction of chemotactic drift. (Kaupp and Alvarez 2016).

*Signaling pathway in A. punctulata sperm.* The signaling pathway involves a chemoreceptor guanylate cyclase (GC - Singh *et al.* 1988) located along the sperm flagellum (Bönigk *et al.* 2009), a sodium/proton exchanger and three different ion channels (Strünker *et al.* 2006; Kaupp and Strünker 2017) to generate the voltage and  $\text{Ca}^{2+}$  response. Binding of resact activates the GC and starts the synthesis of cGMP (Kaupp *et al.* 2003). The ensuing rise of cGMP concentration hyperpolarizes the cell due to the opening of CNGK channels (Strünker *et al.* 2006). This first electrical signaling event is amplified by the subsequent activation of two other signaling components: a voltage-gated sperm-specific sodium/proton exchanger (sNHE) and a hyperpolarization-activated and cyclic nucleotide-gated (HCN) channel (Gauss *et al.* 1998). The sNHE activity causes a small and rapid intracellular alkalinization that shifts the voltage dependence of the sperm-specific  $\text{Ca}^{2+}$  (CatSper) channel to more negative values, thereby leading to the opening of CatSper during the return of the voltage to resting value (Seifert *et al.* 2015). The recovery is initiated by the HCN

channel, which carries a  $\text{Na}^+$  inward current. Recovery from the  $\text{Ca}^{2+}$  response is accomplished by the activity of a sodium/calcium/potassium exchanger (NCKX) and a plasma membrane  $\text{Ca}^{2+}$  ATPase (PMCA) that extrude  $\text{Ca}^{2+}$  from the cell (Su and Vacquier 2002; Gunaratne and Vacquier 2006) and a phosphodiesterase (PDE), which lowers cGMP levels by hydrolysis (Su and Vacquier 2006).

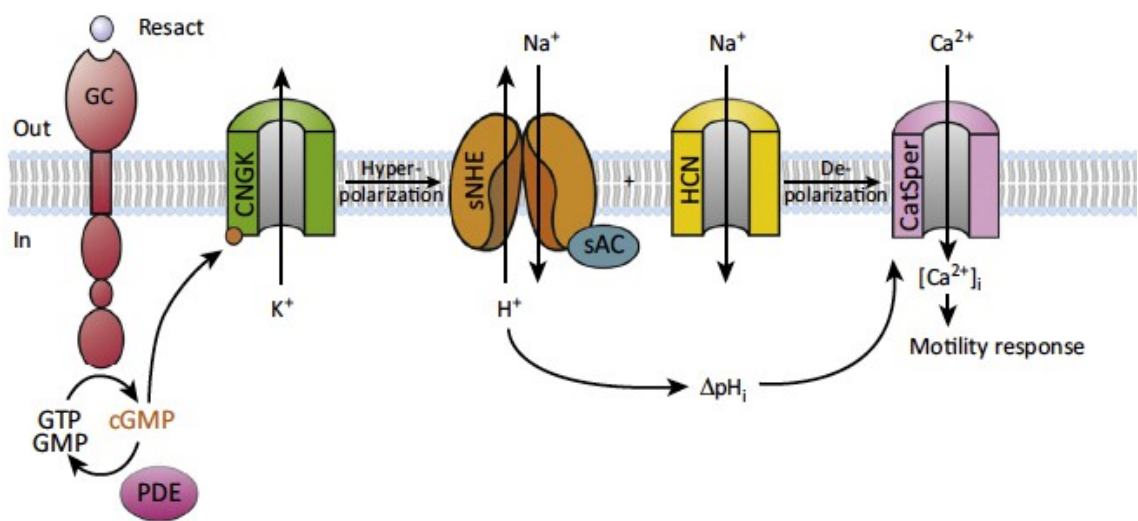


**Figure 4.** Minimal model of signalling pathway controlling chemotactic steering of sperm from *A. punctulata* (see text for details). Binding of the chemoattractant resact to the GC receptor stimulates synthesis of cGMP, which opens CNGK channels and the cell hyperpolarizes ( $V_m$  becomes more negative). Hyperpolarization is followed by intracellular alkalization via a sodium/proton exchanger (sNHE), which shifts the voltage-dependence of the  $\text{Ca}^{2+}$  channel CatSper to more negative membrane potentials. As the cell depolarizes, CatSper channels open and  $\text{Ca}^{2+}$  flows in the cell, which changes the flagellar beat. (Kaupp and Strücker 2017).

Among marine invertebrates, sperm share a similar cGMP-signaling pathway; for instance, sperm of the sea star *Asterias amurensis* also use a peptide as

chemoattractant, a GC as chemoreceptor (Nishigaki *et al.* 1996), and a rapid increase of cGMP concentration that evokes a  $\text{Ca}^{2+}$  response (Matsumoto *et al.* 2003). Differences among species can be observed regarding the swimming behaviour. For example, in a shallow recording chamber commonly used to study chemotactic behaviour under the microscope, sperm from the sea urchin *Strongylocentrotus purpuratus* do not show chemotaxis (Guerrero *et al.* 2010). The hypothesis in this case is that the flagellar beating is restricted by the laboratory conditions of the shallow recording camera, thus no chemotaxis is observable.

*The importance of  $\text{Ca}^{2+}$ .* Although molecules and signal pathways are diverse across phyla,  $\text{Ca}^{2+}$  is the key to sperm navigation.  $\text{Ca}^{2+}$  controls the flagellar beat that steers sperm across the environment of chemical and physical cues toward the egg. Many studies addressed the relationship between the intracellular  $\text{Ca}^{2+}$  concentration ( $[\text{Ca}^{2+}]_i$ ) and the flagellar beat. In the early days of chemotaxis research, the cell membrane of sperm has been treated with detergents to facilitate the adjustment of  $[\text{Ca}^{2+}]$  in the flagellum (Lindemann *et al.* 1991; Lindemann and Goltz 1988). According to these studies, the beat is asymmetrical at high  $[\text{Ca}^{2+}]_i$  and symmetrical at low  $[\text{Ca}^{2+}]_i$ ; consequently, the path curvature should be high (turn) and low (straight swimming) at high and low  $[\text{Ca}^{2+}]_i$ , respectively. However, in intact sperm high  $\text{Ca}^{2+}$  levels persist during straight swimming (Böhmer *et al.* 2005; Wood *et al.* 2005), and the swimming path is adjusted according to the rate of change in  $[\text{Ca}^{2+}]_i$  over time, instead of measuring the absolute  $[\text{Ca}^{2+}]_i$  (Alvarez *et al.* 2014). Furthermore, there is a fundamental need of a model addressing how the flagellar beat steers a cell in a

gradient.

While swimming in a chemoattractant gradient, sperm produce  $\text{Ca}^{2+}$  oscillations in the flagellum (Böhmer *et al.* 2005; Alvarez *et al.* 2012; Kaupp 2012), which is entrained by the periodic stimulation. The  $\text{Ca}^{2+}$  oscillations produce alternating periods of asymmetrical/symmetrical beating. The rapid stimulus oscillations provide a sense of direction, whereas the baseline slope (mean stimulus level) controls the response strength. A positive slope signifying a chemoattractant increase produces weak ‘*on* responses’; a negative slope when losing track evokes strong ‘*off* responses’ (Jikeli *et al.* 2015). The cellular mechanism underlying *on* and *off* responses can be readily revealed by kinetic optochemical techniques (Jikeli *et al.* 2015). The cellular  $V_m$  and  $\text{Ca}^{2+}$  responses have been recorded while sperm, loaded with caged cGMP, were stimulated with pulses of photolyzing light of different length (photolyzing light = to break down molecules with light). The pulses mimic on and off stimulation: when the light is on, cGMP is continuously produced from caged cGMP and the cGMP level is expected to increase steadily, mimicking the rise of the intracellular messenger cGMP during swimming up the chemical gradient. Eventually, a steady-state balance is reached between cGMP production by light and cGMP hydrolysis by the PDE enzyme. When light is switched off, cGMP production ceases and hydrolysis prevails, as it would be expected when stimulation declines during swimming down the chemoattractant gradient; ultimately, cGMP levels rapidly return to resting values. A brief light pulse, shorter than the latency of the  $\text{Ca}^{2+}$  response, produces a normal hyperpolarizing  $V_m$  response followed by a  $\text{Ca}^{2+}$  signal. For long light pulses (i.e. prolonged “cGMP synthesis”), the decline from the

hyperpolarization peak is slower and incomplete. Because CatSper channels open on membrane depolarization, the  $\text{Ca}^{2+}$  responses are smaller compared to the control. After the light is switched off (i.e. when cGMP production ceases), the recovery from hyperpolarization is rapidly completed, giving rise to a second large  $\text{Ca}^{2+}$  off response. The first smaller  $\text{Ca}^{2+}$  signal probably causes smooth helix bending, whereas the second  $\text{Ca}^{2+}$  signal elicits the brisk behavioural off response (Kaupp and Alvarez 2016).

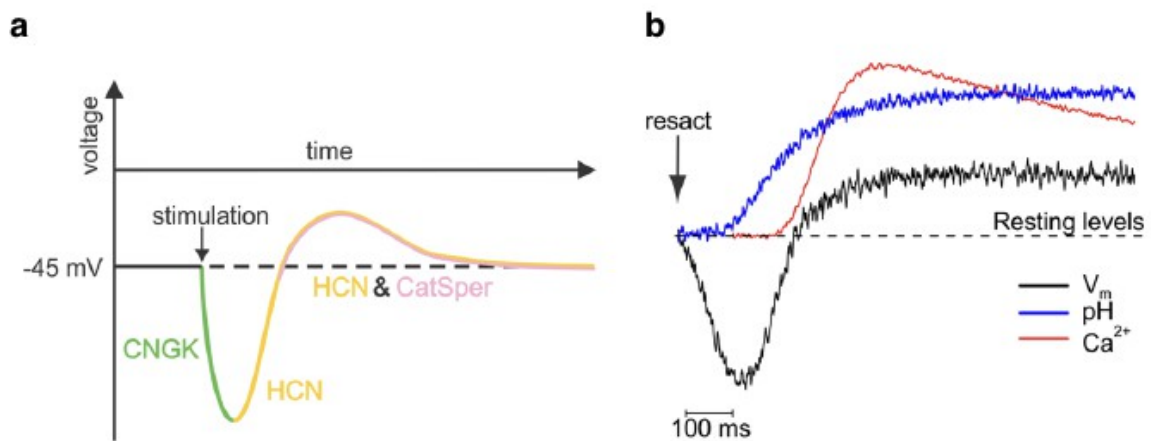


**Figure 5.** Scheme of changes in membrane voltage ( $V_m$ ) upon resact stimulation. a) Contributions of the CNGK, HCN, and CatSper channels are highlighted in green, orange, and pink, respectively (b)  $V_m$ ,  $\text{pH}_i$ , and intracellular  $\text{Ca}^{2+}$  concentration ( $[\text{Ca}^{2+}]_i$ ) after resact stimulation (arrow). Signals were recorded with the fluorescent indicators di-8-ANEPPS ( $V_m$ ), BCECF ( $\text{pH}_i$ ), or Fluo-4 ( $\text{Ca}^{2+}$ ) using the stopped-flow technique. (Kaupp and Alvarez 2016).

### 1.3 The family of guanylate cyclase receptors

*Overview.* There exist two different types of enzymes that synthesize cGMP: soluble guanylate cyclases (GC) and membrane-spanning receptor-type GCs. Receptor-type

GC are ubiquitous across phyla, and several isoforms are known: for instance, mammals have seven GC isoforms known as GC-A to GC-G (Potter 2011); in *Caenorhabditis elegans*, at least 26 isoforms are present (Chen *et al.*, 2005). Receptor GCs serve as chemoreceptors in olfactory sensory neurons and sperm (Dizhoor and Hurley 1999; Meyer *et al.* 2000; Kaupp *et al.* 2003; Potter 2011), but have been also suggested to serve as thermo- and magnetoreceptors in *C. elegans* (Vidal-Gadea *et al.* 2015; Takeishi *et al.* 2016) and thermoreceptors in the Grüneberg ganglion neurons of the nose (Chao *et al.* 2015). In ciliary photoreceptors, which host a cGMP-signaling pathway, receptor GCs are not stimulated by the respective stimulus (i.e. light), but restore cGMP levels after a light response in a Ca<sup>2+</sup>-dependent fashion. Receptor GCs exist in many types of tissue (e.g. smooth muscle, endothelium, heart, adipose, brain, olfactory bulb, retina, testes – for a review see Potter 2011). Chemoreceptor GCs are activated by binding of natriuretic peptides (atrial, B-type, or C-type – Koller *et al.* 1991; Suga *et al.* 1992; Yasoda *et al.* 1998), guanylin, or uroguanylin to an extracellularly located binding site (Hamra *et al.* 1993). Other GCs are activated or inhibited by an intracellular mechanism including carbon dioxide (CO<sub>2</sub>), or bicarbonate (HCO<sub>3</sub><sup>-</sup>) (Chao *et al.* 2010), or carbon disulphide (CS<sub>2</sub>), or guanylate cyclase activator proteins (GCAPs) (Dizhoor *et al.* 1994; Gorczyca *et al.* 1994; Palczewski *et al.* 1994; Dizhoor *et al.* 1995).

Receptor GCs share a topology that consists of three functional domains: a) an N-terminal extracellular domain that binds the ligand, b) a single transmembrane domain (TMD) that divides the protein roughly into two equally large parts, and c) a C-terminal intracellular domain (Kuhn 2003). The intracellular domain encompasses

a kinase homology domain (KHD), which shows similarity to a domain in the family of tyrosine protein kinases, a helical coiled-coil structure known as dimerization domain (DD), which is conserved throughout the GC family and is important for the oligomeric structure, and most importantly the catalytic domain (CD) that is highly conserved in all GCs.

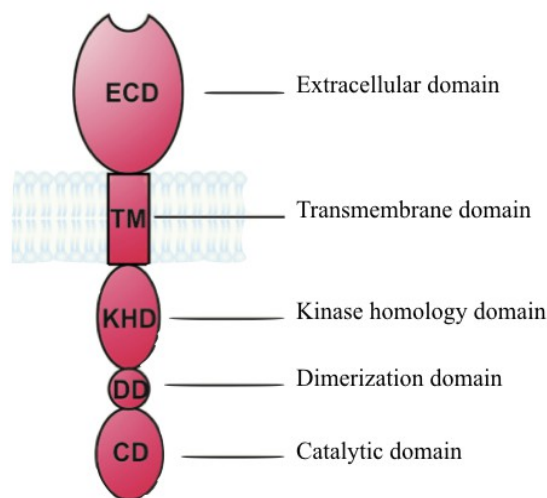


**Figure 6.** General structure of membrane GCs. The GC consists of the following domains: extracellular domain (ECD), transmembrane domain (TM), kinase-homology domain (KHD), dimerization domain (DD), and a catalytic domain (CD). Adapted figure from Kuhn (2003).

The oligomeric state of receptor GCs is debated: monomers, dimers, and other multimers have been reported (Potter, 2011). Biochemical assays reveal dimers, trimers, tetramers or even larger assemblies (Iwata *et al.* 1991; Chinker and Wilson 1992; Lowe 1992; Vandraager *et al.* 1994; Vijayachandra *et al.* 2000). The GC-G in the nose has been proposed to exist as monomer that forms dimers at lower temperatures and, thereby, becomes active (Chao *et al.* 2015). More recently, single-particle EM images and X-rays structures of the extracellular ligand-binding domain

of the mammalian GC-C show that it forms dimers (van den Akker *et al.* 2000; Ogawa *et al.* 2009). However, these studies were performed on isolated, solubilized protein samples of the extracellular domain; thus the oligomeric state of the full-length receptor in the native membrane is still unknown.

*Ligand affinity and GC density in A. punctulata sperm.* *A. punctulata* sperm can respond to binding of a single resact molecule (Kaupp *et al.* 2003; Strünker *et al.* 2006; Bönigk *et al.* 2009). This high sensitivity relies on the high GC efficacy to capture the chemoattractant. The capture efficacy is based on (1) the GC binding affinity, which is in the picomolar range (Pichlo *et al.* 2014), and (2) the high GC number of about 300,000 copies per flagellum (Pichlo *et al.* 2014).

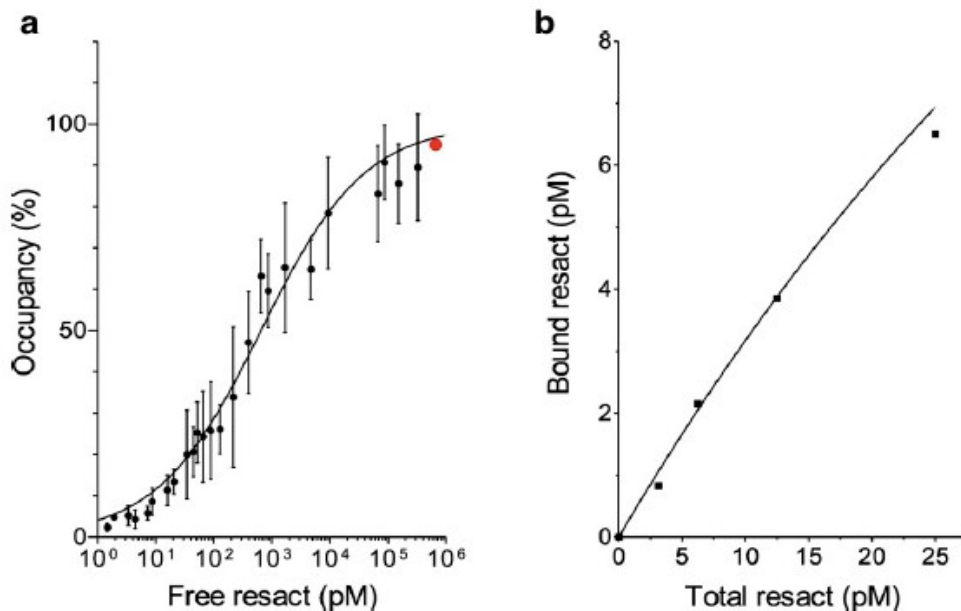


**Figure 7.** Ligand affinity of sperm GC. a) Dose–response relation of resact binding. The continuous line represents a fit of the Hill equation to the data from a total of 126 experiments. Each data point represents the mean  $\pm$  SD of at least three experiments. The constant of half-maximal binding was

$K_{1/2} = 0.65 \pm 0.08$  nM, and the Hill coefficient was  $n = 0.49 \pm 0.03$ . The occupancy at  $\sim 750$  nM resact was set to 95% (31 experiments; red dot). b) Dose–response relation at low resact concentrations. The solid line was calculated using a simple binding model using a  $K_d$  of 250 pM (Pichlo *et al.* 2014).

This high number of GC rivals with rhodopsin in photoreceptors (20,000–45,000 rhodopsin molecules/ $\mu\text{m}^2$ ) as one of the most densely packed membrane receptors (Fotiadis *et al.* 2003; Gunkel *et al.* 2015). What determines the precision by which sperm count molecules?

While the high rhodopsin density ascertains that almost every photon that enters a rod cell is captured, in sperm the high GC density is required to precisely measure changes in ligand concentration. According to the Berg-Purcell limit (Berg and Purcell 1977), the receptor density at a cell surface is one of several parameters that determine the uncertainty  $\partial c/c$  of measuring a concentration  $c$ :

$$\partial c/c = (N_R s D c \tau)^{-1/2},$$

wherein  $N_R$  refers to the number of receptors,  $s$  is the effective radius of the binding site,  $D$  is the diffusion constant of the chemoattractant, and  $\tau$  is the sampling time (Berg and Purcell 1977). With 300,000 GC molecules/flagellum (Pichlo *et al.* 2014),  $\partial c/c$  can be calculated using the following parameters:  $N_R = 3 \times 10^5$  receptors (Pichlo *et al.* 2014),  $D = 2.4 \times 10^{-6}$   $\text{cm}^2/\text{s}$  (Kashikar *et al.* 2012),  $c = 1$  pM (Pichlo *et al.* 2014), and sampling time  $\tau = 0.5$  s (Kaupp *et al.* 2003). The dimension  $s$  of the binding site is not known, therefore the upper and lower limits were defined by the radius of the extracellular GC domain (2.65 nm) and the radius of the resact peptide (0.65 nm), respectively (Pichlo *et al.* 2014). The result indicates that the number of

molecular hits can be measured with a precision of about 13% (Pichlo *et al.* 2014). Therefore, even at a very low concentration of resact, *A. punctulata* sperm are able to count individual binding events (Pichlo *et al.* 2014).

The high GC density is beneficial for a second reason. In the Berg-Purcell model, receptors can be reused within few milliseconds after dissociation of the ligand from the binding site. However, the high ligand affinity of the GC in the sub-nanomolar range prevents receptors from releasing the ligand quickly (Pichlo *et al.* 2014). Consequently, during their travel towards the egg, sperm suffer a continuous loss of functional receptors; thus, a high receptor density is fundamental to ensure a sufficient number of functional receptors even at high ligand concentrations as, for example, near the egg (Kashikar *et al.* 2012).

Despite the importance of the GC density, an accurate value is missing. In fact, previous studies of GC density in flagella of sea urchin sperm yielded mixed results using different techniques: the number of receptors spans from 8,000 GC molecules/flagellum (Shimomura *et al.* 1986) to 60,000 GC molecules/flagellum (Nishigaki and Darszon 2000), to 300,000 GC molecules/flagellum (Pichlo *et al.* 2014).

*Supramolecular organization of receptors in sensory systems.* Aside from the density, the distribution and supramolecular architecture of chemoreceptor GCs might affect and contribute to the sensing mechanism. Many studies have reported higher-order structures for chemoreceptor arrays: in bacteria, a hexagonal lattice of trimers-of-dimers chemoreceptors provides a structural template for long-range cooperativity

among receptors (Hazelbauer *et al.* 2008; Sourjik and Armitage 2010). These patches of chemoreceptor arrays are localized at the cell poles (Hazelbauer *et al.* 2008; Sourjik and Armitage 2010); localization at the cell poles has been also reported for chemoreceptors of *Dictyostelium discoideum* amoebae (Swaney *et al.* 2010). The polar chemoreceptor organization is required for efficient spatial sensing of the chemoattractant (Dusenbery 1998). However, as noted above, sperm perform temporal sampling (Kashikar *et al.* 2012). In photoreceptors, rhodopsin forms dimers, which are organized in rows that form tracks aligned parallel to the disk incisure (Gunkel *et al.* 2015). This supramolecular architecture of rhodopsin may serve as a structural platform to organize the spatio-temporal responses (Gunkel *et al.* 2015). In Gunkel *et al.* (2015), by applying particle-based reaction-diffusion simulations to compare the activation kinetics of the G protein transducing in the presence and absence of rhodopsin tracks, it is suggested that the presence of preassembled transducin complexes, a single activated rhodopsin in a track would activate all transducins trapped in this particular track. Because the sizes of the tracks have little variations in the disk, this could explain the experimentally observed uniform single-photon responses in rod cells. These simulations illustrate how a nanostructured arrangement of visual pigments could affect activation of the transducer and support the notion that the nano-organization of the signaling components has a direct effect on the signaling cascade vision.

One more remarkable example of higher-order organization can be found in mammalian sperm, where CatSper channels are organized in four structurally distinct  $\text{Ca}^{2+}$  signaling domains along the flagella (Chung *et al.* 2014). These CatSper

domains orchestrate the timing and extent of the complex phosphorylation cascades, ultimately altering axonemal motions that govern the characteristic asymmetric and high-angle bend of the flagellum during hyperactivated motility (Chung *et al.* 2014).

#### **1.4 Aim**

Neither spatial distribution nor organization has been previously reported for receptor GCs on *A. punctulata* sperm. In my PhD thesis *A. punctulata* sperm is studied with the aim to resolve the supramolecular organization and distribution of GCs in intact sperm flagella by cryo-electron tomography. As mentioned above, the density and oligomeric state of membrane-spanning receptor GCs are debated. The second aim of this thesis is to solve these open questions by performing sub-tomogram averaging analysis. This technique is necessary to resolve single molecules, and thus, in this study, to determine the oligomeric state of GCs *in situ*.

## 2. Materials and Methods

### 2.1 Materials

Chemicals were purchased at Abbott (Hannover), Agar Scientific (Essex, England), Fluka (Steinheim), Merck (Darmstadt), Roth (Karlsruhe), and Sigma Aldrich (Steinheim). Materials for electron microscopy sample preparation (e.g. grids, filter papers, tweezers) were delivered by Cell Microscopy Core (Utrecht, Netherlands), Electron Microscopy Science (Pennsylvania, USA), Engineering Office M. Wohlwend GmbH (Sennwald, Switzerland), Evident Technologies Inc (New York, USA), FEI (Eindhoven, Netherlands), Plano (Wetzlar).

Buffers were prepared with double distilled water and, when necessary, water was autoclaved (20 min, 121 °C, 1 atm).

### 2.2 Sample preparation

*A. punctulata* sea urchins were obtained from the Marine Biological Laboratory in Woods Hole (Woods Hole, MA, USA), kept in artificial sea water (ASW - 10 mM Hepes pH 7.8, 423 mM NaCl, 25 mM MgSO<sub>4</sub>, 22.94 mM MgCl<sub>2</sub>, 9.27 mM CaCl<sub>2</sub>, 9 mM KCl, 0.1 mM EDTA) at approximately 14 °C and fed with marine plants. The harvesting of sea urchins sperm was done by injecting approximately 1 mL of 0.5 M KCl into the coelom. Additionally, the ejaculation was stimulated by applying a current of 25 V. Sperm cells were then collected in an eppendorf tube using a pipette and stored on ice. The concentration was approximately  $3 \cdot 10^{10}$ - $1 \cdot 10^{11}$  sperm cells/mL.

### **2.3 Sample preparation for electron microscopy**

Having a diameter compatible with vitrification, whole sperm were plunge/frozen, keeping them in a close-to-physiological state. Quantifoil R2/1 holey carbon grids were glow-discharged to make them hydrophilic. This treatment facilitates spreading of the sample droplet on the grid, which provides a constant ice thickness and homogeneous distribution of sperm and, thereby, improves sample quality. The grid was fixed in tweezers and placed in a Vibrobot plunge-freezing machine (Mark IV, FEI, Eindhoven, Netherlands). Immediately prior to vitrification, dry sperm were diluted 1:10 in ASW, and then mixed 10:1 with a colloidal suspension of 10-nm protein-A gold particles (10 mM phosphate buffer saline, pH 7.4, 20% v/v glycerol, 1% w/v BSA, 15 mM sodium azide) (CMC, Utrecht, The Netherlands). The gold particles are used as a fiducial marker that facilitates projection alignment during tomography reconstruction. For activated sperm, samples were incubated with a 100  $\mu$ M resact and incubated for 30 minutes before vitrification. Finally, a 4- $\mu$ L droplet of the final solution was applied onto the carbon-coated side of the grid, followed by blotting to remove excess water. To avoid compression and regulate the process, a filter paper soaked with ASW was used. The following parameters were used for blotting: 5 s waiting time, 6 s blotting time, -3 blotting force, 100% humidity. The grid was then immediately plunged into liquid ethane and collected in a grid box, and stored in liquid nitrogen until imaging. For imaging in the electron microscope, grids were placed in an autogrid (FEI, Eindhoven, Netherlands) and fixed with a clip ring

(c-clip). This procedure was done inside the cryo-chamber of a microtome cooled down to  $-160^{\circ}\text{C}$  (Leica Microsystems, Wetzlar).

## 2.4 Cryo-electron tomography

Grids were transferred to a Titan Krios TEM (FEI, Eindhoven, The Netherlands) operating at 300 kV, and equipped with a Cs-corrector, a Quantum GIF energy filter (Gatan), and a direct detection device (DDD) (Falcon II, FEI, Hillsboro, USA) custom-installed behind the GIF (Fig. 8). The Cs-corrector was used to introduce counter-aberrations to compensate for aberrations introduced by the GIF, resulting in a distortion-free image; the GIF was used to remove inelastically scattered electrons (filter slit-width of 20 eV).

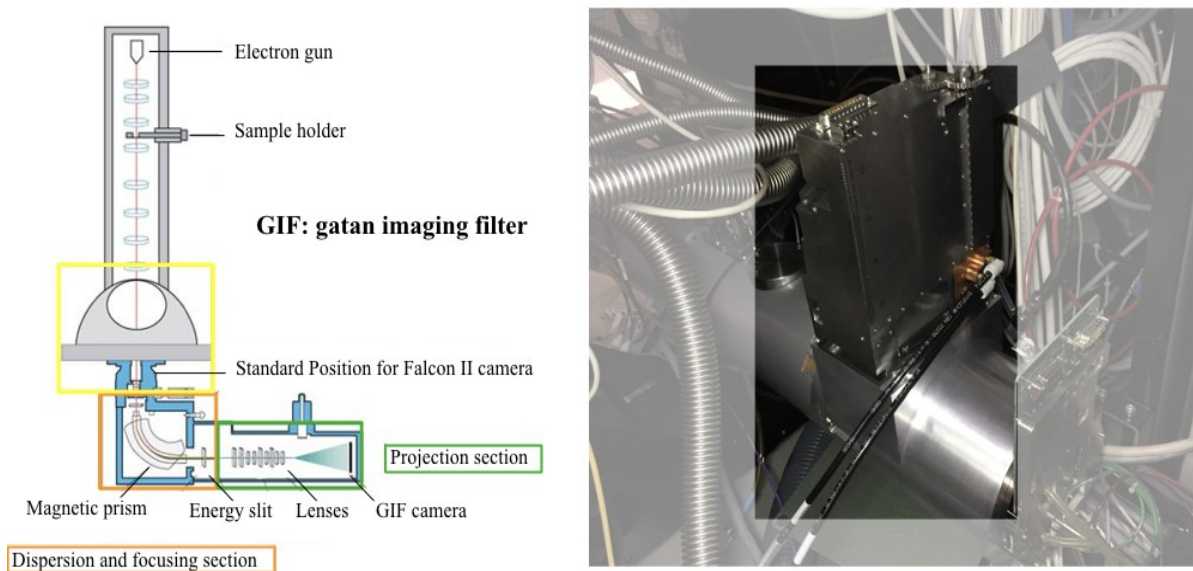


**Figure 8.** Scheme of TEM equipped with a Quantum GIF energy filter. On the left, a schematic representation of a TEM is showing the standard position of a Falcon II camera, the magnetic prism and energy slit which composed the energy filter, and the new position of the Falcon II camera intended now as GIF camera and located after the energy filter. The energy filter consists of two main

parts: a) a magnetic prism: in the curved magnetic field, electrons with different energies are dispersed, and consequently an Electron Energy Loss spectrum is obtained at the end of this part; b) an optical column. An energy range is selected by a slit located at the dispersion plane. In imaging mode, electrons of the selected energy pass through the lenses of the optical system, and an energy-filtered image occurs at the end of the GIF, where a camera is installed for image recording. On the right, a picture showing the Falcon II camera installed behind the GIF in the Titan Krios TEM used for the present studies.

Samples were initially screened under low-dose conditions to identify regions of interest. In these regions, tomograms were recorded using the SerialEM software (Mastrorade, 2005) at 11,500x nominal magnification corresponding to a calibrated pixel size of 5.9 Å. The defocus was set to -4.0 µm. Samples were tilted from -65° to +65° with tilt increments of 1.5°. The total accumulated dose of each tomogram was less than 80 electrons/Å<sup>2</sup>. Tomograms were acquired at different regions along the whole flagellum (see Fig. 12 in Results).

*Data acquisition by SerialEM.* Computer software helps to automatically collect the data. The acquisition requires a sequence of operations, which are affected by imperfections in the goniometers, specimens holders, but also specimen itself (grid not perfectly flat or, in case of sections, the section itself might not be perfectly attached to the grid and thus not flat). Computer control allows limiting these imperfections. In case of tomography, after tilting to a new angle, the feature of interest must be recentered in the field of view, and any change in vertical height must be compensated by refocusing, before the final image is acquired (Mastrorade 2005). The automated

image acquisition helps to precisely track and align the feature of interest, quickening the whole data collection. Thus, the total dose used during the experiment is reduced and the specimen will be less damaged by the irradiating electron beam. SerialEM is a program intended to provide a tool for efficient acquisition, but also an interface for image capture, display and storage. For tomography of beam-sensitive specimens such as frozen-hydrated material, the standard approach is to take focus and tracking images at a location displaced from the area of interest along the tilt axis (Dierksen *et al.* 1993; Nickell *et al.* 2005; Rath *et al.* 1997). SerialEM provides up to four different “areas”, and each of the four sets of camera parameters (called View, Focus, Trial, and Record) is linked to one of these areas. Each area can have an independent magnification, beam intensity, and spot size. However, due to microscope set up with the energy filter, I used the same parameters for these four areas. The area “View” is intended to provide a low-exposure view centered on the area of interest. The “Focus” and “Trial” areas are meant to be offset along the tilt axis. These areas are used for refocusing after tilting and tracking back the position of the object of interest. To record my data set, the focusing and tracking areas were positioned 4  $\mu\text{m}$  offset along the tilt axis. High-quality images are finally recorded on the “Record” area. Before to start with the tomogram acquisition, the eucentricity has to be estimated precisely: this parameter is important to minimized specimen movements during tilt series, and it use the image shift to make the effective optical axis coincide with the tilt axis (Ziese *et al.* 2002; Ziese *et al.* 2003; Zheng *et al.* 2004). Once the desired magnification for the recording is defined, I checked if the area selected for acquisition was suitable for tomography by tilting the grid from  $-65^\circ$  to  $+65^\circ$  making sure that there was no grid

bar coming in at high tilt. Finally, the dose has to be calibrated, and the parameters for acquisition such as defocus, range of tilting, and tilt increments have to be set up. After starting, the tomogram acquisition will run automatically until completion. The data set is then saved as .st file, while the parameters used for acquisition are saved as .mod file; these two files were then used for tomogram reconstruction.

## **2.5 Alignment and 3D reconstruction of tomograms**

Tomograms were first coarsely aligned by the *etomo* software (Mastronarde 1997) using gold particles as fiducial markers. Gold particles helped keeping focus and making tracking more accurate during acquisition of the tilt series, producing tomograms with an alignment error of less than 1 nm. Only tomograms with minimal alignment errors (between 0.3 and 0.5 nm) were selected for further processing. A minimal alignment error indicates that the frozen sample was not distorted under the electron beam during recording. Reconstructions were initially calculated using weighted back-projection algorithms (Mastronarde 1997), and final reconstructions by the simultaneous iterative reconstruction technique (SIRT) algorithm (Gilbert 1972; Guo and Chen 2012). SIRT reconstructions were used for localization of the repetitive pattern of thread-like densities across the width of the flagellum, while back-projected reconstructions were used for the refined sub-tomogram analysis and classification.

## **2.6 Sub-tomogram averaging**

For sub/tomogram averaging, only 3D reconstructions were used in which the lipid

bilayer of the plasma membrane was resolved. 3D reconstructions, recorded along the whole flagellar length, were used for the analysis of the supramolecular organization of the GC. On these reconstructions, sub-tomograms with a size of  $56^3$  voxels were manually selected and extracted from regions corresponding to the plasma membrane. Sub-tomogram alignment and averaging with missing-wedge compensation was performed with the PEET software (Cope *et al.* 2011) as following. Sub-tomograms were initially rotationally aligned assuming that translational shifts of sub-tomograms were approximately correct. For each sub-tomogram, either two (Phi and Theta corresponding to rotation around y- and z-axes) of the Eulerian angles that define the orientation of the reference particle were determined by systematic search over some specified range of values, with the range and the coarseness of the search being reduced in successive iterations of the search (Bostina *et al.* 2007). The third angle (Psi angle corresponding to the x-axis) was scanned during the alignment procedure (Al-Amoudi *et al.* 2007). Absolute values of cross-correlation were used for alignment; this can help prevent noise from reinforcing to match features in the reference (Cope *et al.* 2011). Two different procedures were performed for the alignment. First, to obtain high accuracy, sub-tomograms containing three different couples of GC dimers were extracted from the reconstructed tomograms, aligned, and averaged in 3D. Second, to improve the resolution of each individual GC dimer, sub-tomogram volumes containing only one GC dimer were extracted ( $30^3$  voxels), allowing to focus the alignment on the extracellular domain of the receptor. Isosurface visualization and water shed segmentation were accomplished using the Chimera software (Pettersen *et al.* 2004). In order to fit in the so-called gold-standard

procedures, the sub-tomogram analysis was also performed using the RELION software (data not shown - Scheres 2012). This program was originally designed for single-particle analysis (Bai *et al.* 2015), but a protocol for sub-tomogram averaging from cryo-electron tomography data was recently developed (Bharat and Scheres 2016). For RELION I could make use of sub-tomogram volumes already created for the analysis by PEET software. Thus, tomographic reconstructions and coordinate files of the extracted sub-tomograms were copied into a new directory for processing by RELION and creating a RELION-type metadata (.star format - Hall 1991; Scheres 2012). Parameters used during tomogram acquisition (e.g. voltage, magnification, pixel size) and sub-tomogram extraction (e.g. box size) have to be inserted in the user-friendly GUI of RELION before starting the processing. The analysis is fully automated and it will start first with a 2D classification, followed by a 3D classification and a refinement step before to finally obtain a 3D volume with the particle of interest.

## **2.7 Statistics**

*A. punctulata* animals were harvested during three annual reproductive cycles. Sperm samples collected from different animals were used for data acquisition. From these samples, more than 200 tomograms were recorded from different regions of the sperm flagellum. All the data set acquired revealed a repetitive pattern of thread-like densities across the width of the flagellum. The best 12 tomograms (see Fig. 12 in Results) with a resolution high enough to resolve the lipid bilayer were chosen to calculate the structural values, which are given as mean  $\pm$  standard deviation s.d.

( $n = 12$  tomograms). In details, after sub-tomogram averaging analysis, the sub-volumes with box size  $30^3$  voxels were used to measure the dimensions of a GC dimer (width, height, depth, and distance between two dimers in the same stripe); the sub-volumes with box size  $56^3$  voxels were used to measure the parameters of the helical organization (inclination angle, helical turn, and pitch), the distance between GC stripes, and to calculate the GC density.

## **3. Results**

### **3.1 Cryo-electron tomography of the intact flagellum**

Cryo-ET is a powerful technique for studying the 3D architecture of tissue or the arrangement of macromolecular complexes. Typically, vitrified tissue samples are cut into ultrathin sections of 40-100 nm in thickness to achieve a high signal-to-noise ratio (SNR) and thus high resolution. However, the flagellum diameter is only 250 nm; therefore, sectioning is impractical and might alter the organization of the GC protein in the membrane. Thus, to determine the GC organisation along the flagellum unperturbed by sectioning, we used well-preserved, intact sperm.

However, even if the 250 nm diameter of the flagellum is too thin for sectioning, it is still rather thick for analysis by cryo-electron tomography. Image quality relies on the thickness of the cell and the ice layer (Fig. 9). To ameliorate image degradation due to specimen thickness, an energy filter was used to remove inelastically scattered electrons (Fig. 10).

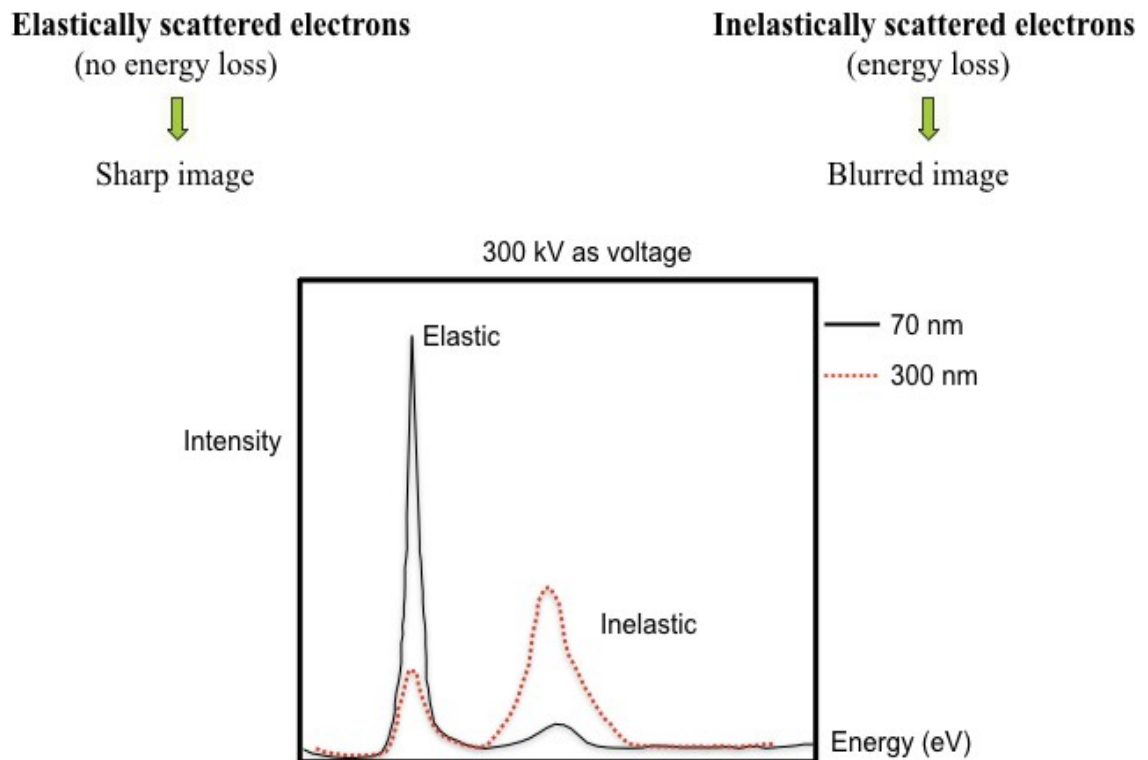


**Figure 9.** Scheme of elastically and inelastically events and their contributions to image quality depending on sample thickness. When the electron beam interacts with the sample we are going to have two different scattering events: elastic and inelastic. In the TEM the portion of the electron beam absorbed is minimal. To be absorbed, an electron must lose all its energy to the specimen. Those electrons which give up part of their energy are said to be inelastically scattered, whereas those which give up none of their energy when scattered are said to be elastically scattered. The amount of scattering which occurs at any particular specimen point is dependent on its density and overall thickness, so that increasing the thickness of the sample will increase the inelastic scattering.



The ice thickness on compressed and uncompressed samples was measured using the following equation:

$$T = \Lambda \ln \left( \frac{I_{tot}}{I_0} \right)$$

in which T, representing the ice thickness, is given by  $\Lambda$  (lambda), which is a constant equal to 320 nm and depends on the voltage of the microscope, multiplied by the natural logarithm of the ration between the intensity of an image acquired without the use of the energy filter ( $I_{tot}$ ) and the intensity of an image acquired using the energy filter ( $I_0$ ). As it is shown in Fig. 11, by adjusting the blotting parameters in order to obtain the best ice thickness suitable with the diameter of the flagellum, I was able to avoid the compression of the flagellum, reaching, eventually, the 90% of sample without compression.

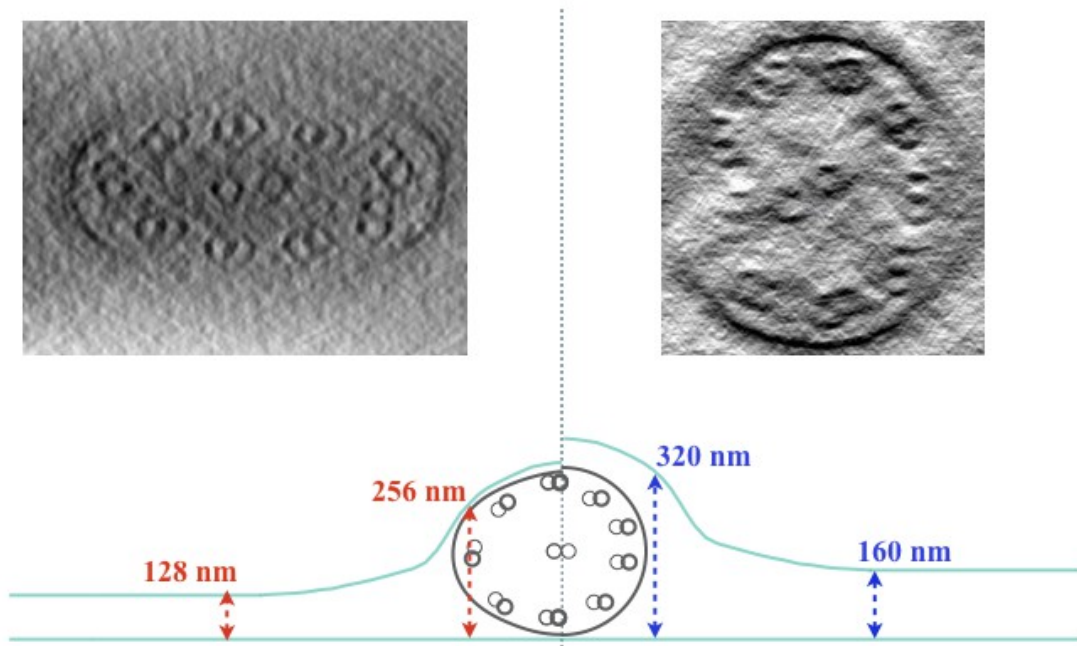


**Figure 11.** Micrographs and scheme showing the ice thickness effect on the compression of the flagellum. On the left, the micrograph shows a highly compressed flagellum. On the right, the micrograph shows an uncompressed flagellum suitable for electron microscopy analysis. A schematic representation on the ice thickness embedding the sample is shown for both the cases.

More than 200 tomograms were acquired. *A. punctulata* animals were used to collect sperm samples with a concentration of  $3 \times 10^{10}$  cells/mL. From each sperm sample, about 15-20 grids were prepared. The flagellum of about three to five cells on a grid was oriented almost parallel to the tilting axis. From these cells, tomograms were acquired from different regions of the flagellum. For further analysis, since the GC is embedded in the plasma membrane, only 3D reconstructions were used in which the lipid bilayer of the plasma membrane was resolved (Fig. 12).

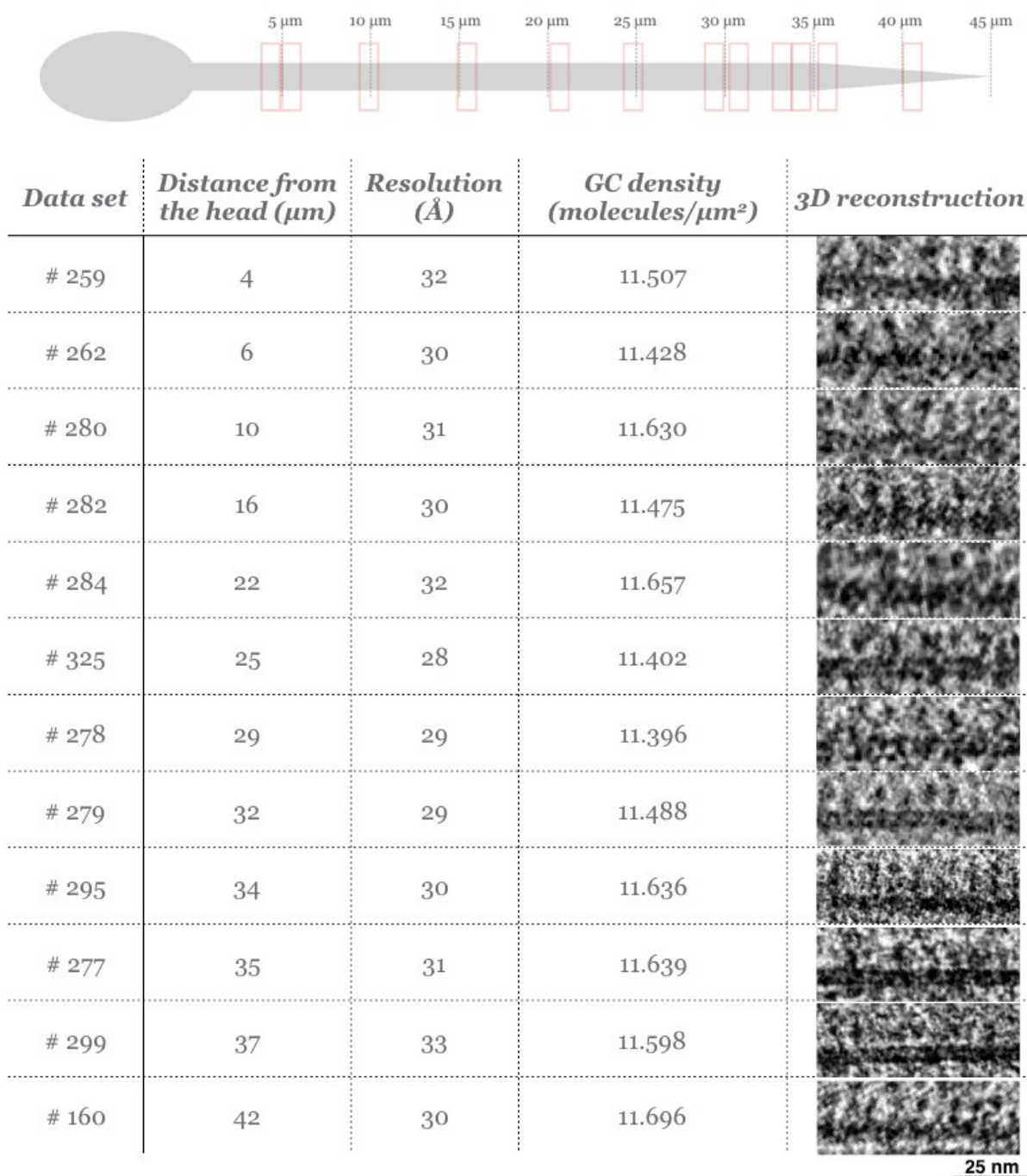


**Figure 12.** Scheme of tomogram acquisition along the flagellum of a sperm cell from *Arbacia punctulata*. The location of the tomogram and the spatial resolution are indicated. For each flagellar region, representative 3D reconstructions show the thread-like structure emanating from the membrane surface. These data sets were chosen for measurements and statistics of structural values for GC density and helical organization, and dimensions of a GC dimer.

To help with the analysis of electron-density distribution along the cylindrical-shaped flagellum, we define the following coordinate system: the y-axis represents the major axis of the flagellum, the x-axis is orthogonal to the y-axis, and the z-axis represents the direction of the electron beam (Fig. 13). The 3D reconstruction reveals a repetitive pattern of thread-like densities across the width of the flagellum (Fig. 14). Because the GC is the most abundant protein in the flagellar membrane (between 5,100 and 8,500 molecules/ $\mu\text{m}^2$ ) (Pichlo *et al.* 2014), we assign these densities in the tomograms to the GC chemoreceptor. Furthermore, being the repetitive pattern of thread-like densities homogeneously distributed along the whole flagellum (Fig. 12) and present in all the analysed samples, this indicates the remarkable robustness of the GC expression during spermiogenesis, accordingly to the fact that sperm are transcriptionally and translationally inactive (Kopf 2002; Asano *et al.* 2010; Han *et al.* 2010).

The observed thread-like densities correspond to the extracellular domain (ECD) of GCs (Fig. 12), while no density is present for the corresponding intracellular catalytic domain (CD). For this reason, I decided to focus the subsequent analysis on the ECD (e.g. Fig. 12).

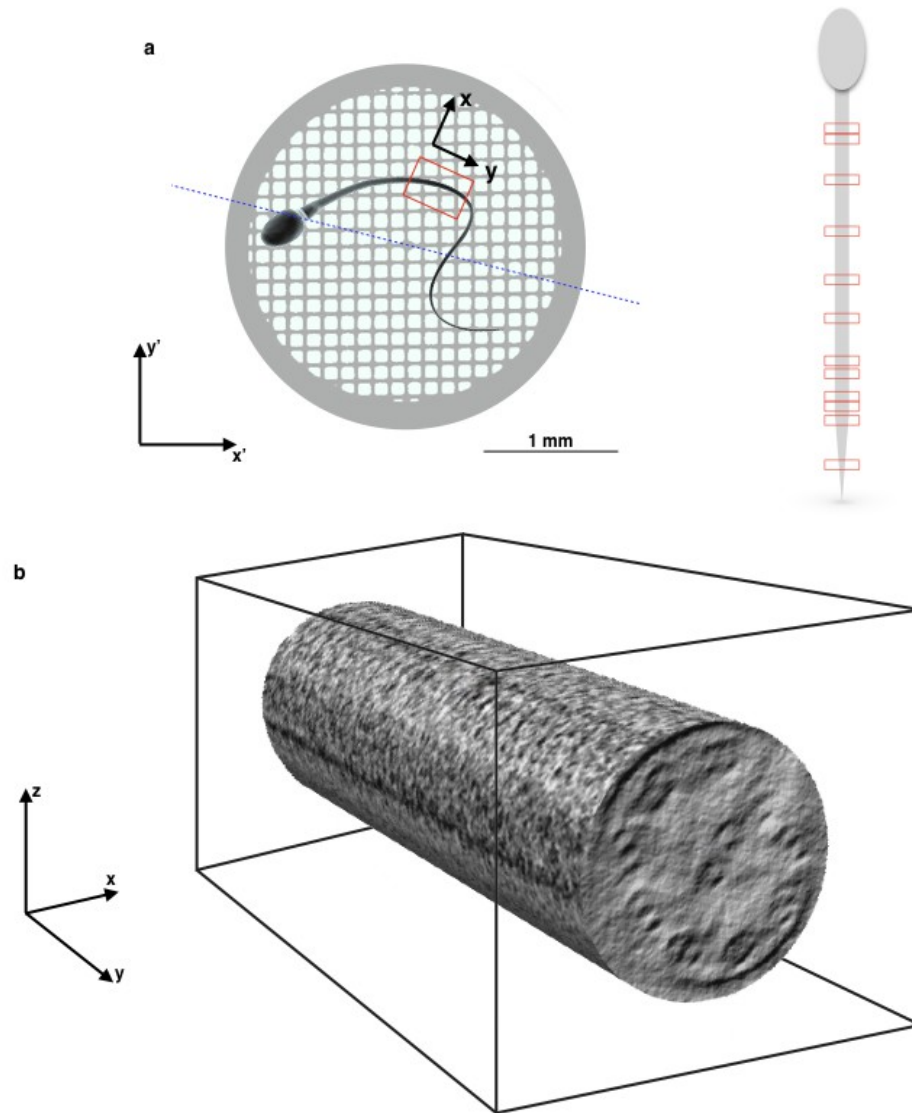


**Figure 13.** 3D analysis of sperm flagellum and GC arrangement by cryo-electron tomography. (a) Scheme of an EM grid and a sperm cell. The coordinate system of the grid is indicated by  $x'$  and  $y'$ . The sperm coordinate system is as follows: the  $y$ -axis represents the major axis of the flagellum, the  $x$ -axis is orthogonal to the  $y$ -axis, and the  $z$ -axis represents the direction of the electron beam. The tilt axis of the EM is indicated by dashed blue line. Tomograms were acquired from regions (red) where the  $y$ -axis of the flagellum runs approximately parallel to the tilting axis. Red boxes on the schematic sperm cell shown on the right indicate the positions along the flagellum from which tomograms have been taken and analysed. The precise positions are given in Figure 12. (b) Representative 3D reconstruction of a flagellum fitted in a cylindrical shape. Longitudinal and cross sections are defined by the  $x$ - $y$  plane and the  $x$ - $z$  plane, respectively.

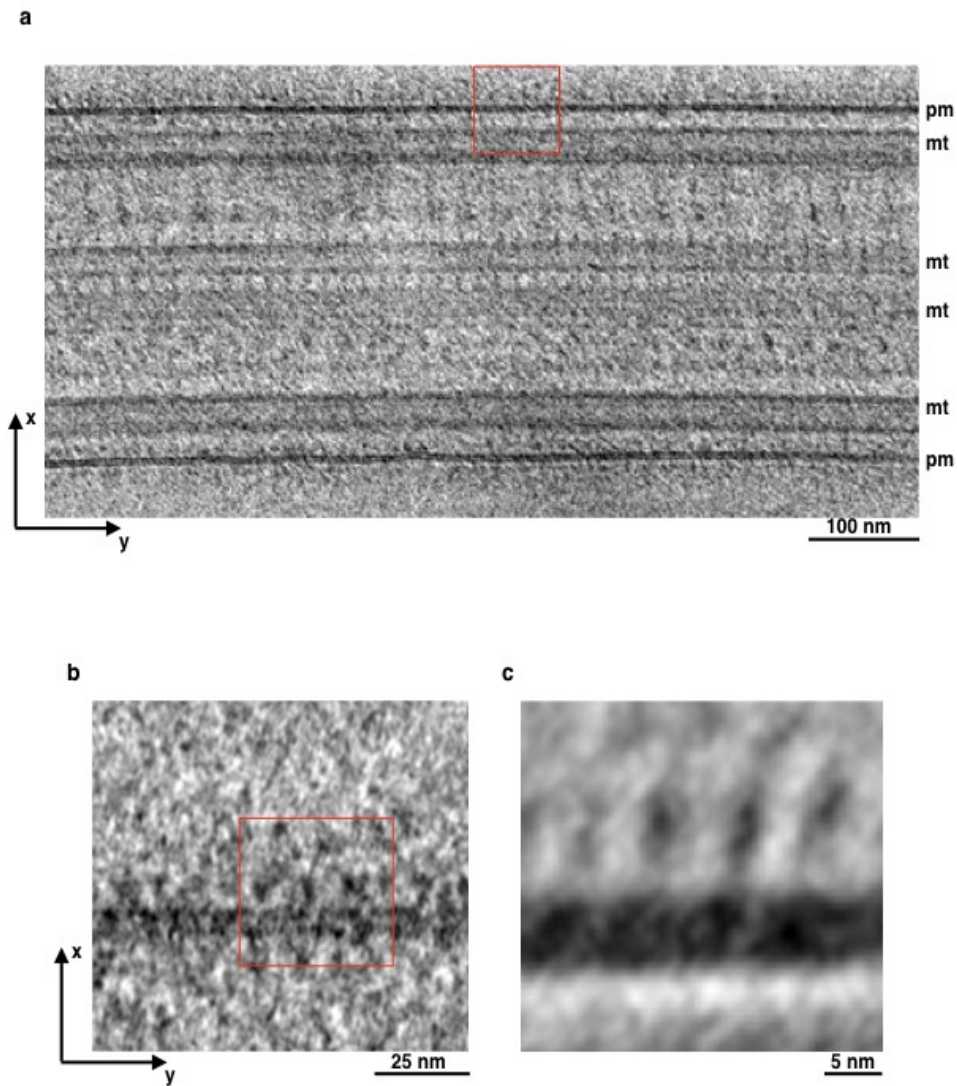


**Figure 14.** 3D analysis of sperm flagellum and GC arrangement by cryo-electron tomography. (a) Tomographic slice through a 3D reconstruction. The 2D image shows a longitudinal section of the flagellum. White and black arrowheads indicate plasma membrane and microtubules, respectively. (b) Enlargement of the boxed area in (a) reveals a thread-like structure emanating from the membrane surface (red box). (c) Front view of GC densities averaged from 400 translationally and rotationally aligned sub-tomograms (red box from part (b)).

To understand if my object of interest (GC stripes) is similar among different volumes, I used the Fourier Shell Correlation (FSC), which measures the normalised

cross-correlation coefficient (CCC) between two 3D volumes over corresponding shells in Fourier space. An FSC curve for data with identical features should appear as a smooth curve (meaning no jumps which indicates distortions or misalignments), with values close to 1 in low frequencies, followed by a semi-Gaussian fall-off and drops to zero; at high frequencies it is expected an oscillation around zero (these are the frequencies more disturbed by noise). For GC data, I have analysed the FSC of 3D volumes to which I either not applied any kind of mask (Fig. 15a), or applied a mask (Fig. 15b) to central feature, which is in this case the central GC stripe on the volume. From the FSC curves it is possible to see that alignment and fitting of the GC stripes from different volumes were good. Thus, I could assume that the GC stripes are similar over the whole length of the flagellum. Accordingly, I could proceed with the analysis of the ECD densities considering the overall organization as a constant.

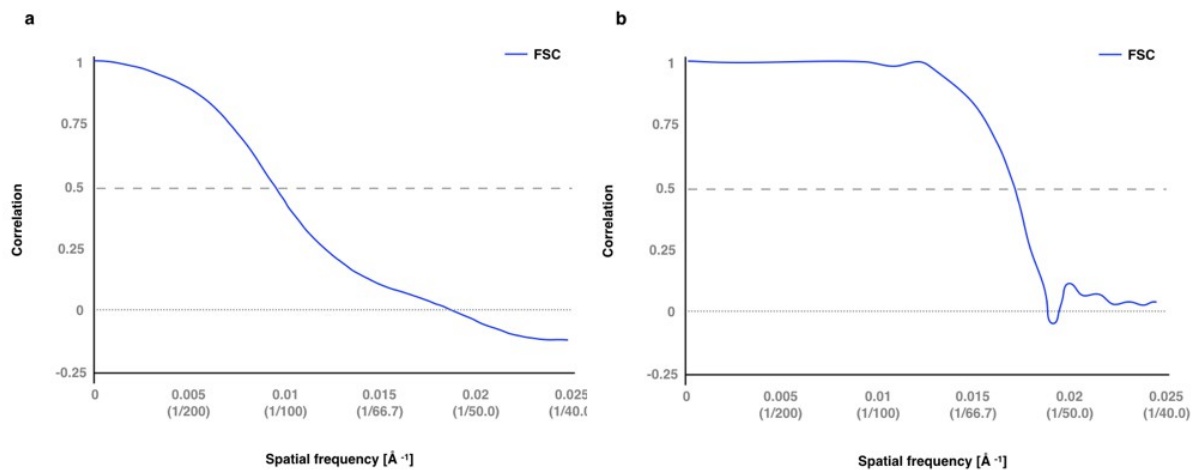


**Figure 15.** Fourier Shell Correlation of sub-tomogram volumes. FSC curves were calculated for 3D volumes of GC densities obtained by sub-tomogram average. The plot in a) shows the FSC curve of volumes to which no mask was applied. The plot in b) shows the FSC curve of volume to which mask was applied. Spatial frequency and correlation values are shown on the x and y axis, respectively.

### 3.2 The GC is organized as a helix that coils around the flagellum

From each tomogram, more than 300 sub-tomograms (box size  $56^3$  voxels) of the thread-like structures on the flagellar surface were extracted. To enhance the signal-to-noise ratio, sub-volumes were translationally and rotationally aligned and averaged; this procedure allowed analysing the structures at the molecular level. The analysis shows that GC chemoreceptors are arranged in parallel stripes (Fig. 16). The stripes are tilted with respect to the x-axis of the flagellum (Fig. 17). The stripes could represent either a tilted stack of rings or a helix that coils around the flagellum. To distinguish between these two arrangements, we compared sub-tomograms from both sides of the same flagellum. The rows from opposite sides displayed an inverted inclination with respect to the x-axis (Fig. 16), indicating that the stripes coil around the flagellum in a helix-like fashion.

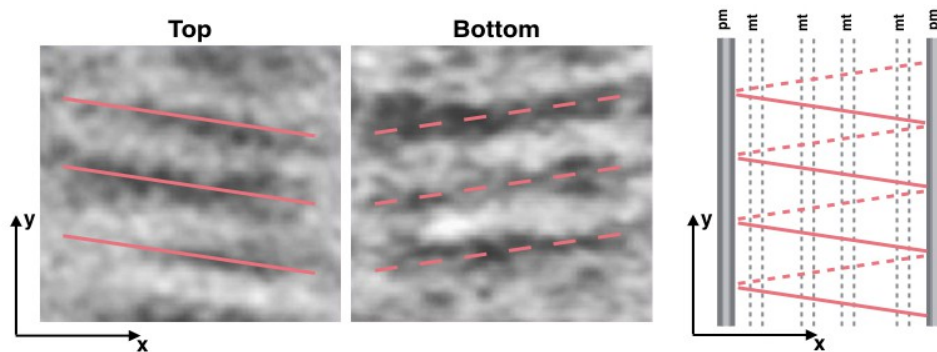


**Figure 16.** Geometric arrangement of GC stripes in sperm flagellum. Tomographic slices through a 3D reconstruction showing projections of GC densities from opposite sides of the flagellum (referred to as top and bottom). The stripes from opposite sides display a mirror-inverted inclination with

respect to the x-axis, suggesting that the GC densities coil around the flagellum in a helix-like fashion. Right: schematic representation of the GC stripes (continuous lines top and dashed lines bottom of the flagellum). Plasma membrane and microtubules are indicated as pm and mt, respectively.

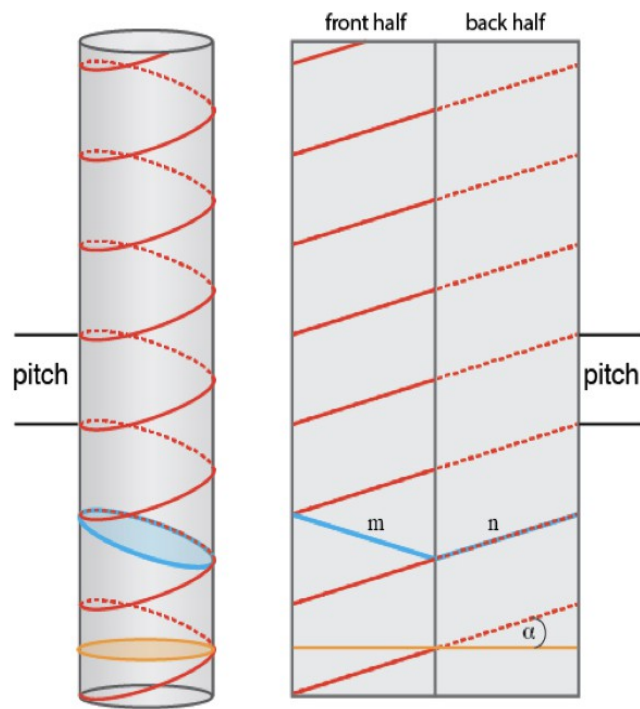


**Figure 17.** Helical parameters of the GC arrangement in the sperm flagellum. Scheme showing the geometrical parameters of the GC stripes with regard to the flagellum cylinder (left) and with regard to the unwrapped surface (right). Stripes are tilted with an angle  $\alpha = 15.5 \pm 0.5^\circ$  with respect to the x-axis; the pitch of the helix is  $6.0 \pm 0.2$  nm. The length of a helical turn ( $2n$ ) is identical the perimeter ( $n+m$ ) of an ellipse (blue) that is tilted by an angle  $\alpha$  with respect to the circular x-z plane (orange).

We determined the geometrical parameters of the helix. The stripes are organized as a left-handed helix from the head to the tip of the flagellum with a pitch (distance between neighbouring turns) of  $6.0 \pm 0.2$  nm. The stripes are inclined with an angle  $\alpha$

=  $15.5 \pm 0.5^\circ$  with respect to the x-axis. Accordingly, the length of a helical turn can be approximated by the perimeter of an  $\alpha$ -tilted ellipse around the flagellum. The ellipse perimeter is given as:

$$2\pi \sqrt{\frac{\left(\frac{A}{2}\right)^2 + \left(\frac{B}{2}\right)^2}{2}}$$

wherein A refers to the minor axis of the ellipsoid (equivalent to the flagellar diameter  $2r$ ) and B refers to the major axis (which is  $A/\cos \alpha$ ). For  $r = 0.125 \mu\text{m}$  and  $\alpha = 15.5^\circ$ , the perimeter becomes  $\sim 0.8 \mu\text{m}$  (Fig. 16 and Table 1).

Parameters	Values
Dimension of ECD of a GC dimer	width $7.5 \pm 0.5 \text{ nm}$
	height $8.5 \pm 0.5 \text{ nm}$
	depth $3.0 \pm 0.5 \text{ nm}$
Distance between dimers in a stripe	$3.0 \pm 0.3 \text{ nm}$
Distance between two stripes	$6.0 \pm 0.2 \text{ nm}$
Plasma membrane thickness	$6.6 \pm 0.3 \text{ nm}$
Helix pitch	$6.0 \pm 0.2 \text{ nm}$
Helix circumference	$0.8 \mu\text{m}$
Tilt angle $\theta$	$15.5 \pm 0.5^\circ$
Flagellar radius	$0.125 \mu\text{m}$
Flagellar length	$45 \mu\text{m}$
Flagellar surface	$35 \mu\text{m}^2$
GC density	133 dimers/helical turn
	$11,546 \pm 150 \text{ molecules}/\mu\text{m}^2$
	$404,109 \pm 5249 \text{ molecules}/\text{flagellum}$
	$26 \pm 0.35\% \text{ flagellar surface covered}$

**Table 1:** Structural parameters of ECD dimers and helix organisation. The dimensions of the GC dimers and stripes were derived from averaged data.

### 3.3 The GC forms dimers

Different stoichiometries of GC oligomers have been reported. The extracellular ligand-binding domain (van den Akker *et al.* 2000; Ogawa *et al.* 2009) forms dimers. Biochemical assays including cross-linking techniques reveal dimers, trimers, and tetramers (Iwata *et al.* 1991; Chinker and Wilson 1992; Lowe 1992; Vandraager *et al.* 1994; Vijayachandra *et al.* 2000). These studies were performed on isolated solubilized protein samples. To identify the oligomeric structure *in situ* in native membranes, we analysed sub-tomograms using two different box sizes ( $30^3$  and  $59^3$  voxels – Fig. 18a) and focusing on individual repeat units; thereby, we reached molecular resolution and were able to solve the oligomeric state of the GC.

As mentioned before, the analysis is focused on the ECD of the GC dimer. Since the intracellular domain of the GC dimer is not visible in our data (Fig. 12), I used the ECD for sub-tomogram alignment and average. Even after averaging, no significant density was present for the CD.

To optimize alignment parameters on a single-repeat unit, density contributions from adjacent stripes were removed using a cylindrical mask around the central stripe (11 nm diameter, 100 nm width) (Fig. 18b).

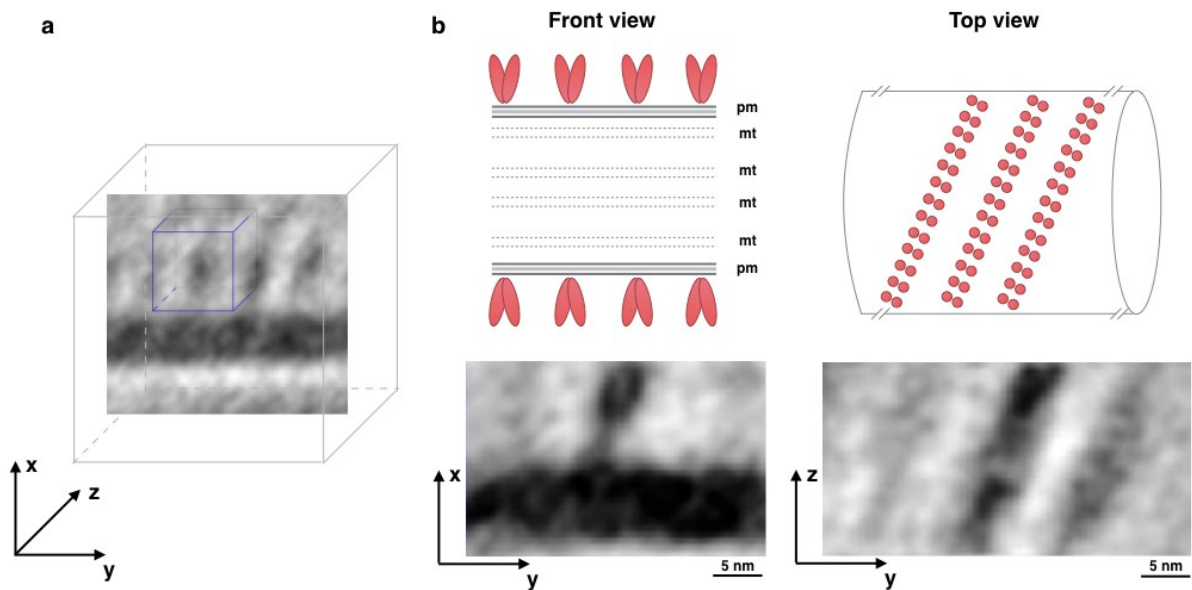


**Figure 18.** Low-resolution analysis of GC stripes. (a) Scheme showing the relation of the sub-tomogram volume used for identifying the higher-order organization ( $56^3$  voxels; 33.2 nm side length) with respect to the sub-tomogram volume used for molecular identification of the ECD densities ( $30^3$  voxels; 17.8 nm side length). (b) Front view and top view of 400 translationally and rotationally aligned and averaged sub-tomograms ( $56^3$  voxels) of ECD densities. Schematic representation of the flagellum, the dimeric receptor (red), and its supramolecular organisation is shown above each sub-tomogram slice.

Next, we restricted the alignment to the extracellular receptor domain (box size  $30^3$  voxels) to avoid potential misalignment due to contributions from the featureless plasma membrane (Fig. 19).

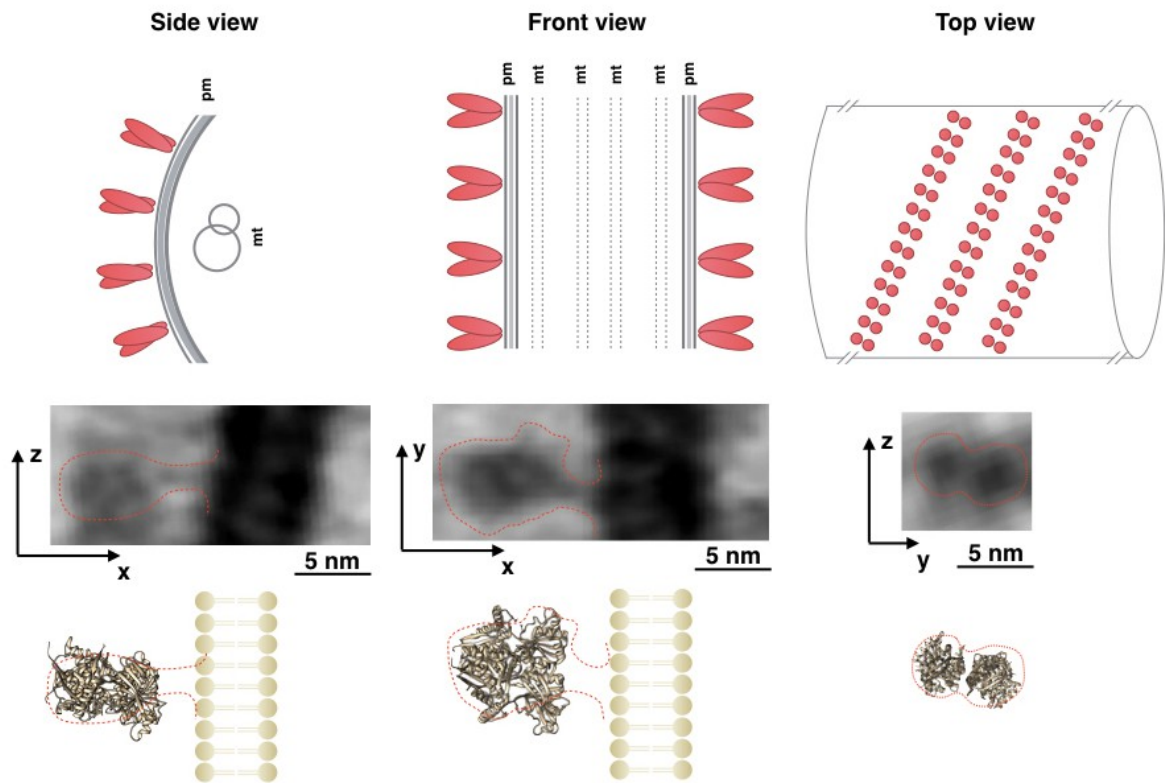
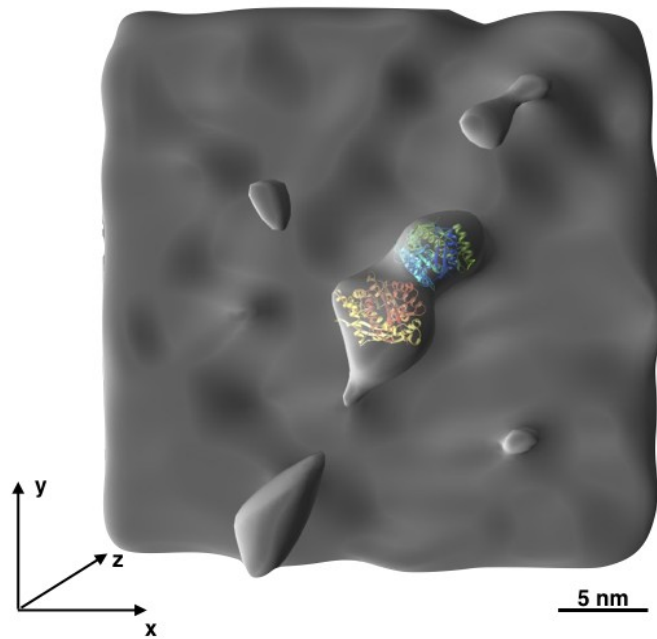


**Figure 19.** High-resolution analysis of GC stripes and ECD dimers. Side, front, and top views of 400 translationally and rotationally aligned and averaged sub-tomograms ( $30^3$  voxels) of ECD dimers. Schematic representation of the flagellum, the ECD dimers (red), and their organisation is shown above each sub-tomogram image. The respective views from the crystal structure of an orthologue receptor (Ogawa *et al.* 2009) are shown to scale below the corresponding sub-tomogram image. All images are provided with the respective coordinate system and scale bars. pm, plasma membrane; mt, microtubules.

Thereby, we achieved a resolution sufficient to distinguish between densities that represent the monomers in a ECD dimer (Fig. 20).

**Top view**



**Front view**

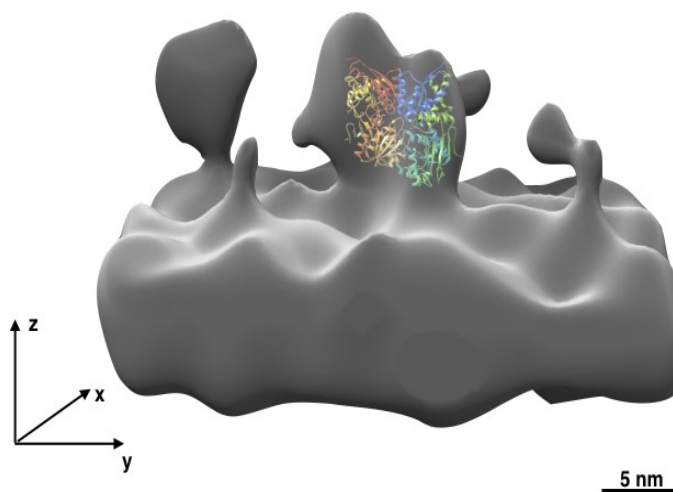


**Figure 20.** Three-dimensional structure of the extracellular domain of a ECD dimer. Isosurface representation (front and top views) of the sub-tomogram average of the ECD in a GC dimer (grey volume). Running at an inclination of  $15^\circ$  are two additional densities corresponding to the preceding and following ECD of a GC dimer in the coil. Running parallel to the central ECD volume are two weak densities corresponding to the ECD of GC dimers from the preceding and following pitch of the coil. Two copies of the extracellular domain of the natriuretic peptide receptor, an orthologue receptor

of GC, can be fit into the central GC volume (PDB ID: 1yk0). The two copies are indicated using red-to-yellow and blue-to-green, respectively; dark colors (red and blue) indicate the N-term region, while light colors (yellow and green) indicate the C-term one. The images are provided with the respective coordinate system and scale bar.

Thus, we could build a model of the overall organisation (Fig. 21).

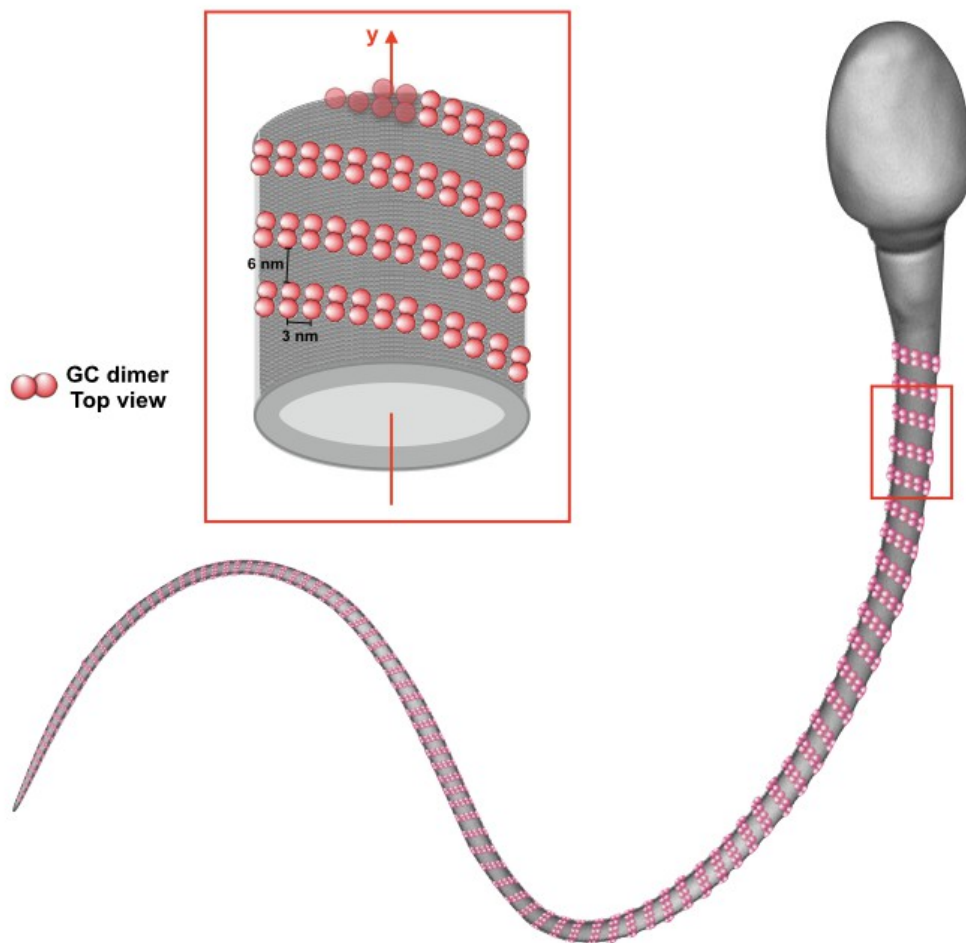


**Figure 21.** Model of the GC organization in a sperm flagellum. The model shows an overview of the GC (red) organization in a intact flagellum. Two levels of organization are shown: dimerization of GC monomers; dimers form a long stripe that coils around the whole flagellum in a helix-like fashion. Enlargement of the boxed area in the flagellum shows the magnified top view of GC dimers (red) organized as stripes.

The same analysis of GC activated by the chemoattractant resact (Fig. 22) confirmed the preservation of the helical higher-order architecture (Fig. 21). After GC activation and thus during sperm swimming, only a small difference in the distance between two stripes has been reported. The distance between two activated GC stripes appeared slightly increased (from  $6.0 \pm 0.2$  nm  $6.7 \pm 0.2$  nm) in regions where the curvature of the bending was high, while in regions where the bending was irrelevant there was no detectable change in the distance between stripes. This effect is due to the properties of a helical structure: for straight helix (as in the case of a flagellum in rest state), the helix makes a constant angle (the pitch angle) with the horizontal plane (here the y axis of the flagellum). This is not the case for a bent helix where the tangent of the bent flagellum makes an angle with the diameter of the flagellum itself in that point (for review on theoretical analysis about helix bending, turns, and switch, please see Olsen and Bohr 2012). Therefore, the pitch angle becomes function of the tangent, and it will be approximately constant for small bending, but it will increase for high bending as in the case of a flagellum during swimming. In practical terms, the effect on GCs stripes will be that in regions where the curvature of the bending is high, it is expected a higher pitch angle and, consequently, an increased distance between stripes, while in regions where the bending is irrelevant the distance between GCs stripes is expected to be approximately the same as in resting state.

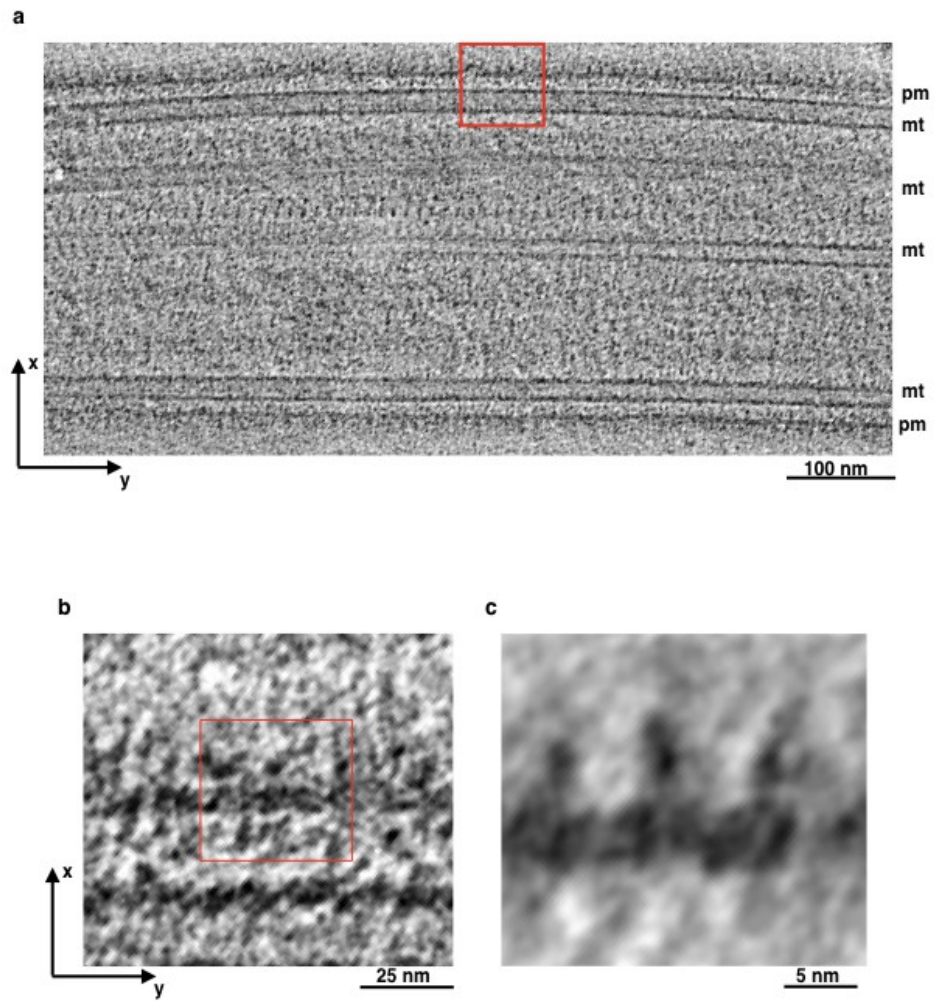


**Figure 22.** 3D analysis of sperm flagellum and GC arrangement upon resact activation by cryo-electron tomography. (a) Tomographic slice through a 3D reconstruction. The 2D image shows a longitudinal section of the flagellum. White and black arrowheads indicate plasma membrane and microtubules, respectively. (b) Enlargement of the boxed area in (a) reveals a thread-like structure emanating from the membrane surface (red box). (c) Front view of ECD densities averaged from 400 translationally and rotationally aligned sub-tomograms (red box from part (b)).

The size of a ECD dimer is:  $7.5 \pm 0.5$  nm width,  $8.5 \pm 0.5$  nm height, and  $3.0 \pm 0.5$  nm depth (Table 1). The distance between two dimers in a stripe is  $3.0 \pm 0.3$  nm. The dimer dimensions are consistent with the size of the extracellular domain of a

homologous receptor determined by single-particle EM (9 nm width, 8 nm height, 5 nm depth - 22 Å resolution; Ogawa *et al.*, 2009) or X-ray crystallography (12.5 nm width, 6 nm height, 3.5 nm depth – 2.0 Å resolution; van den Akker *et al.*, 2000).

### 3.4 Structural parameters of GC dimers in a helix

Combining the information from both box sizes of sub-tomograms ( $30^3$  and  $59^3$  voxels – Fig.s 17 and 18), we determined the density of GC dimers in the membrane along the flagellum. Assuming a flagellar surface of  $35 \mu\text{m}^2$  (length  $45 \mu\text{m}$  and radius  $0.125 \mu\text{m}$ ), calculation of the GC density led to a value of  $11,546 \pm 150$  molecules/ $\mu\text{m}^2$  equivalent to  $404,109 \pm 5249$  GC molecules in the whole flagellum (Table 1). Taking into account the area occupied by a GC dimer of  $22.5 \text{ nm}^2$ , the GC receptor covers  $26.0 \pm 0.35\%$  of the flagellar surface (Table 1). Thus, the GC represents one of the most densely packed membrane receptors.

Considering the helix geometry, we calculated the number of GC dimers per turn. The area covered by one turn is  $0.006 \mu\text{m}^2$  (length of a turn  $\sim 0.8 \mu\text{m}$   $\times$  width of a GC dimer  $0.0075 \mu\text{m}$ ). Considering the dimensions of a GC dimer and the dimer-dimer distance, the area covered by a dimer is  $45 \text{ nm}^2$  ( $7.5 \text{ nm} \times 6.0 \text{ nm}$ ). Therefore, one turn is composed of 133 dimers. This value is validated by the theoretical number of GC dimers which is possible to fit in one turn (Fig.23). In fact, GC dimensions determined by single-particle EM are considered (Ogawa *et al.* 2009), any distance between dimers in the same row is assumed, a turn can accommodate a maximum number of 160 GC dimers.

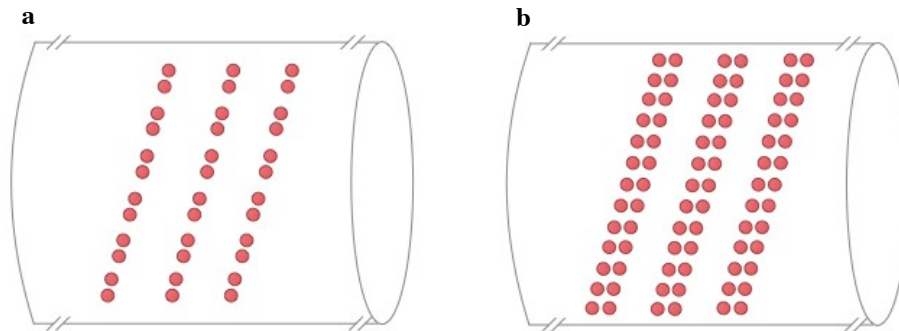


**Figure 23.** Schematic representation of two possible scenarios for the GC dimer orientation within the row. Considering the length of a helical turn ( $0.8 \mu\text{m}$ ), we can estimate the GC density for both scenarios and see if our data fit with one of the models. To calculate the densities, I used the measures calculate by Single Particle (SP: GC width =  $5 \text{ nm}$ ; GC length =  $9 \text{ nm}$ ), and also by X-ray crystallography (Xstl: GC width =  $3.5 \text{ nm}$ ; GC length =  $12.5 \text{ nm}$ ). If we do not consider any distance between two dimers in the same row, and we overfill the helical turn with GC dimers, the numbers are: for (a) GC dimers per turn equal to 89 (SP) or to 64 (Xstl); (b) GC dimers per turn equal to 160 (SP) or to 228 (Xstl). Considering that there will be a distance between GC dimers, the calculated 133 GC dimers per turn from our data fit quite well with (b).

Eventually, analysing the tomograms acquired along the entire length of the flagellum (Fig. 12), it was possible to investigate whether the density and highly-ordered organization of GC are restricted to parts of the flagellum or if they are uniform along the complete flagellar surface. The GC density (Fig. 12), the width of each stripe, and the distance between two stripes (Table 1) are indeed uniform along the whole length of the flagellum. This result suggested that each region of the flagellum has the same probability to capture chemoattractant molecules.

## 4. Discussion

In this Ph.D. thesis, I have studied by cryo-EM the supramolecular architecture of the GC chemoreceptor in the flagellar membrane of intact sperm: GC forms dimers and the dimers form a string that coils around the entire length of the flagellum in a helical fashion. Eventually, I determined the GC density along the flagellum.

In the following, I will organize the discussion in two subsections. In Subsection 1, I will discuss the advantages, but also technical limitations of cryo-EM for the study of the supramolecular architecture of GC.

In Subsection 2, I will discuss the physiological significance of the GC density, its uniform distribution, and the helical organisation. Finally, I will compare my results to previous data obtained by biochemical methods (mass spectrometry and gel densitometry), single-particle electron microscopy, and X-ray crystallography.

### *Subsection 1 - Drawbacks and advantages of cryo-electron tomography*

Aqueous biological samples must be preserved before they can be placed in the high vacuum of an electron microscope. To avoid artefacts due to dehydration (aggregation, deformation, and shrinking) the sample can be either stained with heavy-metals or vitrified. The staining technique is used in conventional EM, however, the stain is imaged rather than the biological material itself. This method is useful in gaining contrast to highlight specimen's characteristics, but also creates

artefacts by the very nature of the staining (Hayat and Miller 1990). To overcome this limitation, I used vitrified samples which are not fixed or stained. The production of high-quality samples for cryo-ET is a matter of perfect vitrification and structural preservation. To achieve vitrification, I applied the plunge-freezing method, obtaining samples that are preserved in a frozen-hydrated state and preventing damage of the specimen's ultrastructure.

For the aims of this project, I planned every experiment (summary in Fig. 24) considering what are the best techniques and methods to solve the specific issues or take advantage from the characteristics of the subject of interest. Biological ultrastructures are intrinsically 3D, so that to study the GC arrangement, it was important to obtain the full 3D volume of the flagella rather than 2D images. Accordingly, I applied cryo-electron tomography (cryo-ET), allowing to obtain detailed 3D structures (Frank 1992; Frank 2006) of sub-cellular macromolecular objects in the flagellum.

To avoid damage during analysis, vitrified samples are imaged with low-dose radiation. The permitted low-dose limits the sample thickness to a range between 40 to 100 nm, because in thicker samples multiple electron-scattering events diminish the resolution and, consequently, acquired images will be extremely noisy. Usually, thick vitrified specimens are cut into ultrathin sections by cryo-sectioning (CEMOVIS). Here, I have to consider the size of the sperm flagellum from sea urchin, which is about 250 nm in diameter, as the limiting factor to obtain samples suitable for cryo-ET analysis. In this study, cross sections of the flagellum would reveal neither the organization nor the distribution of GC proteins because of the

limited area of interest present in such sections. Furthermore, longitudinal sections are difficult to generate due to bending of the flagellum. Finally, sectioning might alter the GC organization of the GC in the membrane and thus creates artefacts (Al-Amoudi *et al.* 2005). Consequently, I could not apply the CEMOVIS technique to study the GC organization, but I had to acquire tomograms on an intact sperm flagellum.

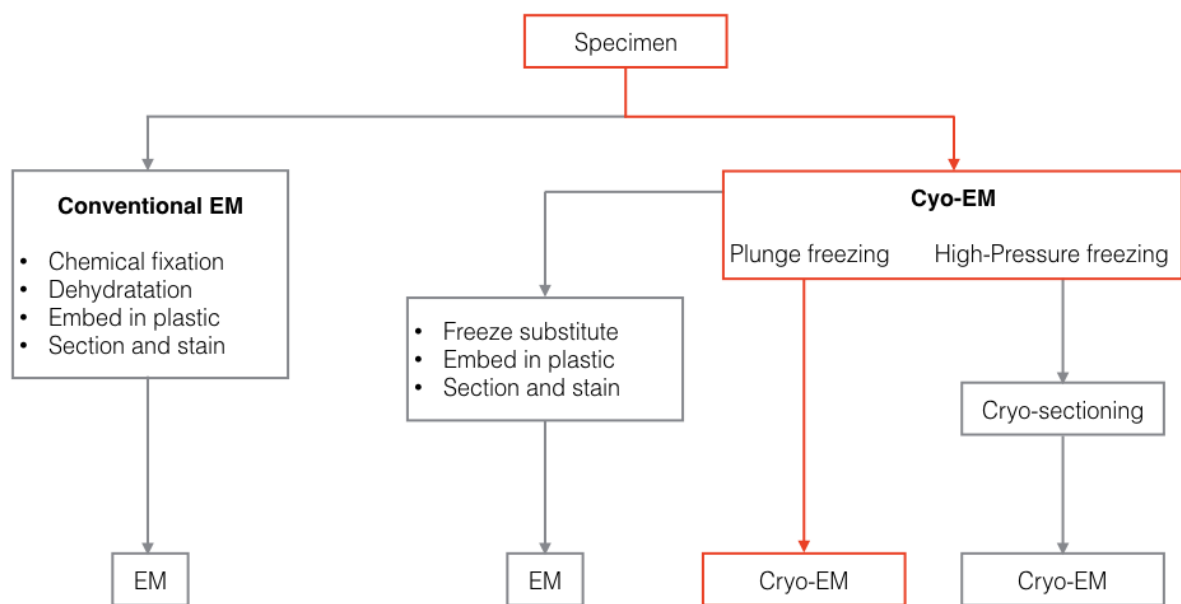


**Figure 24.** Flowchart of specimen preparation for conventional or cryo-EM. The image illustrates the key steps needed for sample preparation. As states before, a specimen can be prepared either for conventional EM (needs of stain) or cryo-EM (no stain needed). Once the sample is ready, it is possible to directly image it in case of the plunge freezing technique, or the sample needs to be sectioned before imaging, as reported for the rest of the possible techniques available either for conventional or cryo-EM.

*The problem of a low signal-to-noise ratio.* Working with a frozen-hydrated sample is advantageous to study close-to-native structures, but it comes at a price. The

unstained specimen is radiation sensitive. Where does this radiation sensitivity originate? In conventional EM, embedding of the sample in a layer of dried staining solution provides some protection: the accessible molecular surfaces are coated with reagents containing heavy atoms that are much less radiation-sensitive than organic matter (Milne *et al.* 2013). In cryo-EM, the damage results from the interaction of electrons with the organic matter of the sample (Frank 2006; Nicastro 2009; Milne *et al.* 2013).

To avoid sample damaging, the sample must be imaged under low-dose conditions, which results in images with a low signal-to-noise ratio (SNR) and also limits the suitable sample thickness (McIntoch *et al.* 2005). Furthermore, in cryo-ET, the total dose is fractionated into smaller amounts per projection; consequently, the images' contrast will be poor, making it difficult to detect features of interest (Frank 2006; Nicastro 2009).

However, if the structure of interest is repetitive and present in multiple copies, the SNR can be significantly enhanced by averaging. By this procedure, the random noise is suppressed, whereas the signal contributions are maintained (Nicastro *et al.* 2006; Heymann *et al.* 2008).

Here, I could take advantage of the high density of GC, which allows discriminating the GC from less abundant proteins. After tomogram reconstruction and sub-tomogram extraction, I aligned and averaged per data set more than 400 sub-tomograms (for details see Material and Methods), increasing the SNR and obtaining meaningful and high-resolution averages of 3D images of GC particles.

*Limits on the specimen thickness.* After tomogram acquisition, the reconstructed volume contains 3D information of the GC molecules. In principle, to obtain a full 3D volume, projections of tilt angles up to  $90^\circ$  have to be acquired (Loos, 2009). In practice, due to hardware limitations of the microscope, the sample can be only tilted up to  $\pm 65^\circ$ . In addition, even using an ideal microscope hardware, a tilted frozen sample has an increased ice and sample cross section (Fig. 25).

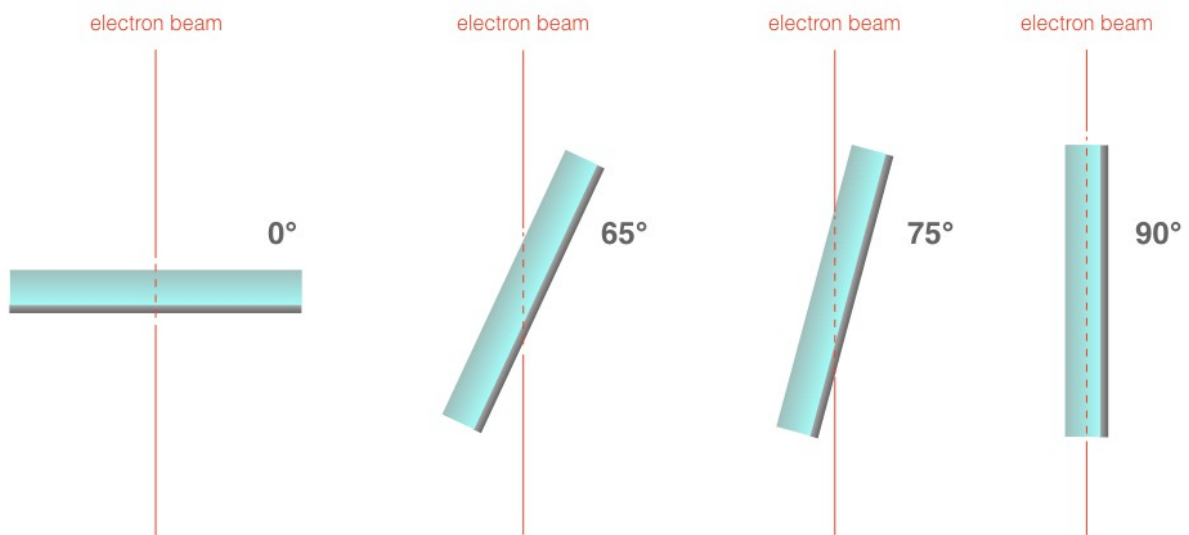


**Figure 25.** Effect of sample tilting on the increase of ice thickness. The image shows how tilting of the sample during tomogram acquisition affects the ice thickness, or mean free-path that electrons cross to reach the camera and produce an image. The longer the distance that electrons have to travel, the higher the probability to get inelastically scattered events that make blurred images of poor quality, as well as sample heating and damage. The length of the path that electrons must travel through the sample mean is indicated by a dashed red line, whereas the electron beam is indicated by a continuous red line. The vitrified specimen is represented in light blue bar, and the grid is represented in grey.

This cross section is the average distance that the electron travels before it is scattered (Egerton *et al.* 2004). As a consequence of the increased thickness, the majority of electrons will not conserve their kinetic energy (inelastically scattered events). This energy loss brings about poor quality images (blurred micrographs), specimen heating, and structural damage (Egerton *et al.* 2004).

To overcome the energy loss related to the sample thickness, the camera used for tomograms' acquisition was positioned behind a GIF energy filter. The energy filter removes inelastically scattered electrons, which mainly contribute to image noise, and allows obtaining images with an enhanced SNR. Thereby, I could analyse a thick sample with a low-electron dose and ameliorating image degradation.

*The missing-wedge problem.* One last limitation to overcome in cryo-ET is the “missing-wedge” problem, i.e. the lack of part of the information within the 3D volume recorded. Each sub-tomogram will have a wedge of missing information in Fourier space as the consequence of 3D reconstruction from a limited range of tilt angles ( $\pm 65^\circ$ ). The missing wedge causes deformations in Fourier space (Fig. 26) and lead to corresponding images in real space that are not isotropically resolved (Förster *et al.* 2005; Schmid and Booth 2008).

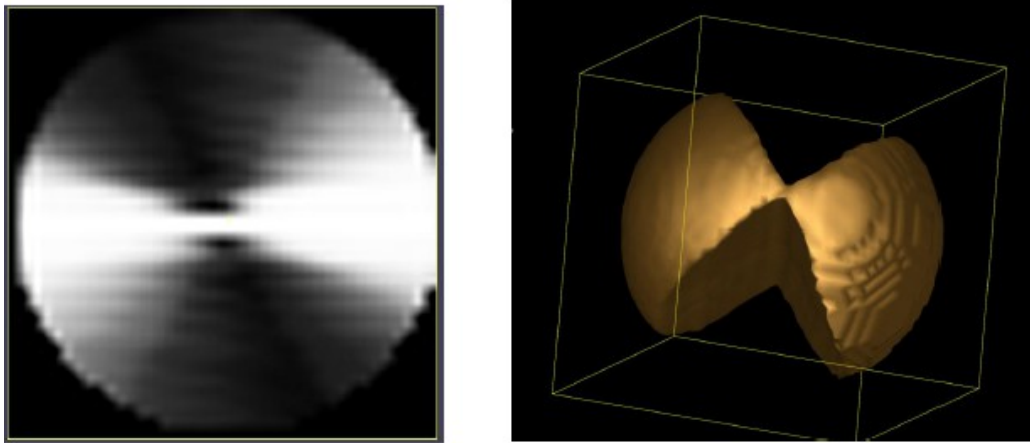


**Figure 26.** Missing-wedge effect in Fourier space. On the left the missing-wedge effect is shown in a grey-level image. On the right the missing-wedge effect is shown in a 3D isosurface representation.

The deformations due to the missing information produce a directional artefact in 3D reconstruction. As a result, features are distorted in the direction that corresponds to the missing information (McIntoch *et al.* 2005); here it is the x-axis in the coordinate system defined for the flagellum. The only direction not affected by the missing-wedge is the electron beam direction (in this study the z-axis).

Different approaches have been used to reduce the missing information: 1) dual-axis ET (Mastronarde 1997; Penczek *et al.* 1995), that is the acquisition and combination of data from two perpendicular tilt axes; 2) in case of an object with a fixed geometry, by single-axis ET it is possible to use the geometry itself to estimate the coarse alignment angles between all selected densities (Heuser *et al.* 2009), also known as sub-tomogram averaging. Taking advantage of the cylindrical geometry of the flagellum, the GC supramolecular architecture is a suitable sample for which it is possible to overcome the missing-wedge problem by combining cryo-ET and averaging. In fact, within the same tomogram, GC densities have different

orientations (Fig. 27a), a higher-order organization, and a repetitive distribution.

Due to different orientations, sub-tomograms will have GC densities each affected by a different missing wedge (Fig. 27b). During sub-tomogram averaging, I defined the axis to which the GC densities have to be aligned. Once aligned, these densities will be averaged to obtain a final 3D volume in which the missing information is restored (Fig. 27c).

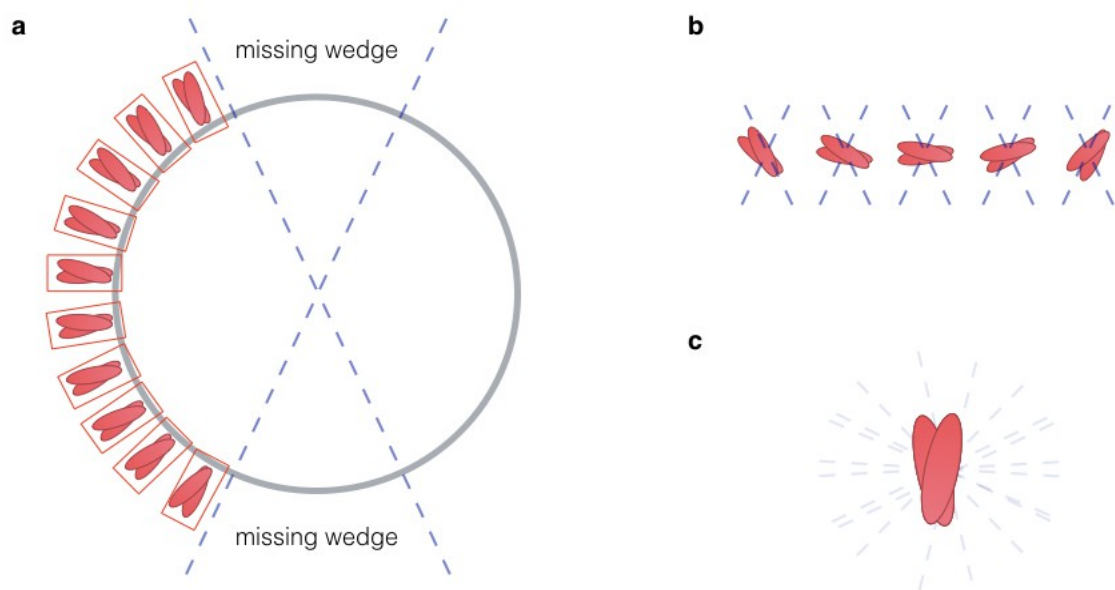


**Figure 27.** Missing-wedge effect on GC particles from sperm flagellum. **(a)** The scheme represents the GC densities positioned on the plasma membrane (grey line) of the flagellum in a cross-section view (x-y plane). The cylindrical shape of the flagellum allows GC to have multiple orientations. **(b)** Single GC densities adopting different orientations and their relative missing-wedge effects are represented. Due to their different orientations within the tomogram, GC densities will suffer from different missing information for each of them. **(c)** The missing information can be filled-in by sub-tomogram averaging: these densities will be combined to obtain a 3D volume in which the missing-wedge effect will be partially compensated. Missing-wedge (dashed blue lines) and sub-tomograms (red boxes) are indicated.

*The analysis of the supramolecular GC architecture avoiding the missing-wedge effect.* As explained in the above paragraph, several technical issues had to be solved to obtain a credible structure not only at the molecular level of the GC dimers, but also avoiding artefacts in their overall architecture. In this work, I report that GC dimers are forming a row which coils around the flagellum in a helical-like fashion. To solve the helical organization, it was necessary to find a method that was not affected by the missing-wedge effect. In the reconstructed 3D volume, only one axis is not affected by the missing-wedge effect: the z-axis, which represents the direction of the electron beam. Accordingly, on the y-z plane is possible to obtain 2D images showing the orientation of GC rows and containing the full information without distortion. I used this 2D images to measure the tilt angle of the GC rows, a parameter which is essential to calculate as precise as possible the overall helical organization. To avoid forcing of alignment of the GC rows, sub-tomogram averaging analysis did not impose any pre-alignment and did not provide any reference (either derived from real data or from simulations). Moreover, averaging was done using a box size of  $56^3$  voxels, which allows observing several GC rows in the same 2D image; thus it is possible to measure the inclination angle of each row. After sub-tomogram averaging, a 2D image on the z-axis plane was analysed, taking care to align the plane of the plasma membrane with the y-axis of the flagellum to avoid distortions of rows. Finally, I built a cartesian system of the x- and y-axes on the 2D image of the GC rows (Fig. 28). Because the flagellum is a cylinder, the

plasma membrane is curved and so the inclination angle of the row must be determined as the angle between the x-axis and the line tangent to the central part of the row, which will be the area less affected by the flagellar curvature. Using this method, I was able to measure a tilt angle of  $\alpha = 15.5 \pm 0.5^\circ$  and calculate accordingly the helical geometry of the row of GC dimers.

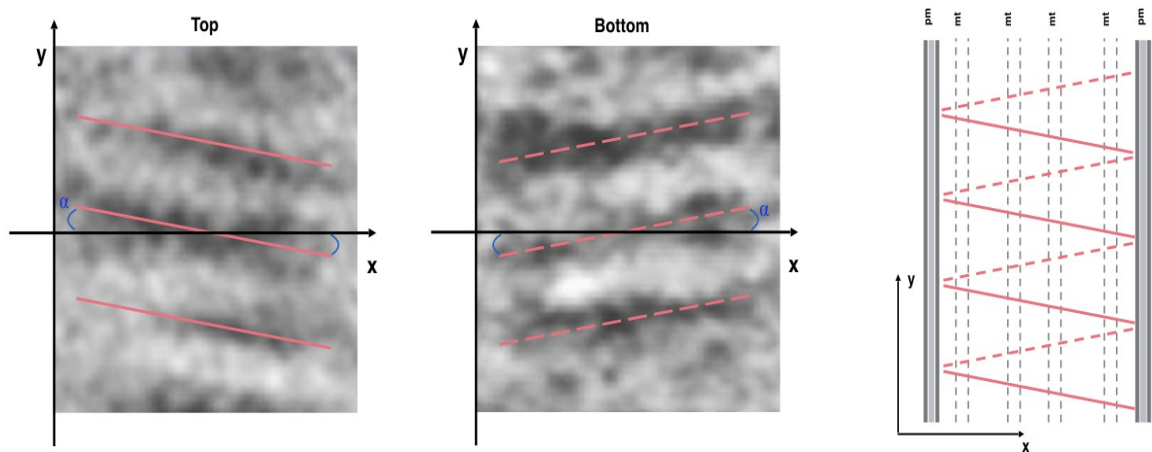


**Figure 28.** Measurements of the tilt angle of GC rows. The images shows the cartesian system of x- and y-axis used to measure the inclination angle of the GC rows ( $\alpha = 15.5 \pm 0.5$ ). Top and bottom indicate the different views of the two sides of the flagellum. As shown, GC rows from opposite sides show an inverted orientation, indication of a helical arrangement. The line tangent to the central part of the GC row was considered to measure the tilt angle. The tangent is indicated a red line (continuous or dashed). At the right side of the image is shown a scheme of the flagellum with the superimposition of the tangents measured from both sides.

## *Subsection 2 – Biological insights from the GC density and its supramolecular architecture*

Prior to discuss findings in terms of biological significance, I have to mention once more that our data show only to the ECD of GCs (Fig. 12), while no density was detected for the corresponding CD. Why the CD is not visible? This effect might be due to the properties of the subject itself. Recent works on the soluble guanylate cyclase (Campbell *et al.* 2014; Gileadi 2014) have shown multiple conformational changes and the flexibility of the CD. Even though soluble GCs and receptor GCs are not identical, the CD is a conserved module; thus, we can hypothesize a similar behaviour in terms of flexibility and conformational changes of the CD. On this base, the flexibility of the CD might not allow a good alignment during processing, and also 3D volumes obtained by sub-tomogram average may not show any CD density. During the analysis, I could not visualise any CD density either on tomograms nor after sub-tomogram average. Thus, I focused the complete analysis on the ECD of GCs, assuming that each ECD corresponds to a full length receptor GC in *A. punctulata* sperm.

*Density of the GC in the intact sperm flagellum.* Previous work reported a GC amount ranging from 180,000 molecules/flagellum to 300,000 molecules/flagellum determined by mass spectrometry and gel densitometry, respectively (Pichlo *et al.* 2014). Here, I determined the GC density along the flagellum. The density is

$11,546 \pm 150$  GC/ $\mu\text{m}^2$ . Assuming a flagellar surface area of  $35 \mu\text{m}^2$ , I estimated a total number of  $404,109 \pm 5,249$  GC/flagellum (Table 1). Thus, the GC density revealed by three different techniques matches reasonably well. The difference between the biochemical methods and cryo-ET might be due to the fact that biochemical measurements rely on calibrations, including standard proteins and counting of sperm in samples (see Pichlo et al. 2014 for more detail). By contrast, the determination of GC density along the entire length of the flagellum by cryo-ET does not rely on such calibration procedures.

What might bias the GC density obtained by cryo-ET? After sub-tomogram averaging, for each region of the flagellum, I calculated the GC density assuming an average surface area of  $1,100 \text{ nm}^2$  (the edge length of each sub-tomogram box is  $33.16 \text{ nm}$ ). Because this calculation is done on averaged images, it will introduce some errors in the overall number (see *Subsection 1* for detail – *The missing-wedge problem*). The alignment during sub-tomogram averaging is complicated by the low contrast and noise present in the EM images. As a result, although the averaged images provide resolution superior to that in the original image, they also introduce a bias, which might lead to an overestimation of the density. However, the fact that the GC density in different regions along the flagellum is similar argues that the imprecision is not large.

*Distribution of GC along the flagellum.* By analysing the tomograms acquired along the entire length of the flagellum (Figs. 12 and 13), it was possible to test whether the

high density or higher-order organization of GC is restricted to particular regions of the flagellum or whether the density is uniform. The density analysis (Fig. 12) involved the width of each stripe and the distance between stripes (Table 1). In fact, the GC density is similar along the entire flagellar surface, except for the end piece. This result implies that the probability to capture chemoattractant molecules is uniform on the entire flagellar surface.

Although the GC distribution is uniform, the efficacy to generate a  $\text{Ca}^{2+}$  response once GC captured a resact molecule might be different. In fact, the signaling components like CNGK or CatSper channels might be unevenly distributed. Further experiments will need to be conducted to answer this question.

*What might be the functional significance of the high density and uniform distribution of GC?* The high GC density (12,000 molecules/ $\mu\text{m}^2$ ) is similar to the density of rhodopsin, the visual pigment in rod photoreceptors (25,000 molecules/ $\mu\text{m}^2$ ) (Gunkel *et al.* 2015; Schertler 2015). In rod photoreceptors, the high rhodopsin density ascertains that almost every photon that enters a rod cell is captured. In sperm, the high GC density is required to precisely measure changes in ligand concentration. As mentioned before, the receptor density at a cell surface is one of several parameters used by the Berg-Purcell model (Berg and Purcell 1977). The uncertainty  $\partial c/c$  determined introducing the GC density that I have calculated in this study ( $N_R = 4 \times 10^5$  receptors - Table 1) indicates that the number of molecular hits can be measured with a precision of about 12.8%, confirming previous findings on the ability of *A. punctulata* sperm to count individual binding events, even at very

low concentration of resact (Pichlo *et al.* 2014). In comparison, bacterial chemoreceptors operate at nano- to micromolar chemoattractant concentrations; therefore, these cells would need a much lower receptor density and, in fact, have a receptor density of about 15,000 molecules/cell (Li and Hazelbauer 2004; Cannistraro *et al.* 2011; Sourjik and Wingreen 2012). A subset of olfactory neurons in the nose of some animals can detect pheromones at femto- to picomolar concentrations (Brennan and Zufall 2006; Zhang *et al.* 2013). It will be interesting to know whether these pheromone receptors in cilia are also arranged at high density and display a supramolecular organization.

A more intuitive way to explain the need of a high GC density considers the very nature of diffusion. In fact, it has to be considered that molecules impinging on a cell are going to wander around the cell surface and eventually be captured by a receptor or leave the cell surface for good. A high receptor density is enhancing the probability that ligand molecules are recaptured after unsuccessful previous encounters.

When considering the reasons behind the high GC density, also the high ligand affinity of the GC must be taken into account. As mentioned before, the ligand affinity is in the sub-nanomolar range and prevents receptors from releasing the ligand quickly. The Berg-Purcell model assumes that receptors are reused within few milliseconds after dissociation of the ligand from the binding site, which is reasonable for receptors with micro- to millimolar affinities and dwell times of ligand on the receptor in the micro- to millisecond range (e.g. bacterial receptors). Therefore, the high GC density is beneficial to ensure that a sufficient number of

functional receptors remains available even at high ligand concentrations present near the egg (Kashikar *et al.* 2012).

*Higher-order organization of GC: a comparison with rhodopsin architecture and bacterial receptor array.* Similarly to rhodopsin in photoreceptors or to chemoreceptors in bacteria, it can be noticed that also sperm rely on a high receptor density. However, the three “sensory” systems have different geometrical organizations: helical coil, tracks, and hexagonal arrangement of trimers-of-dimers.

What might be the functional role - apart from the high density - of different geometric arrangements of receptors?

The supramolecular architecture of rhodopsin dimers, which are organized in rows aligned parallel to the incisure of the disk membrane (Gunkel *et al.* 2015; Schertler 2015) might serve as structural platform to organize the spatio-temporal interaction of signaling molecules, to produce uniform photo-responses, and to detect polarized light (Gunkel *et al.* 2015). In bacteria, the chemoreceptors organized in a hexagonal lattice of trimers-of-dimers provide the structural underpinnings for long-range cooperativity among receptors (Sourjik and Armitage, 2010). In *A. punctulata* sperm, a row of GC dimers regularly coils around the cylindrical flagellum in a helical-like fashion. Previous reports could not find any evidence for positive cooperativity among GC chemoreceptors (Pichlo *et al.* 2014). Moreover, although the high GC density endows the cell surface with a high capture efficacy, the helical arrangement contributes only a small geometric factor, if at all, to the capture efficacy. Thus, the helical organization might serve a different function related to rigidity and elasticity

of the flagellum that affect the bending motions of waves travelling down the flagellum during swimming. To illustrate how the GC organization might influence the flagellar bending, I will use two geometric models: helical and “spaghetti” model (Fig. 29).

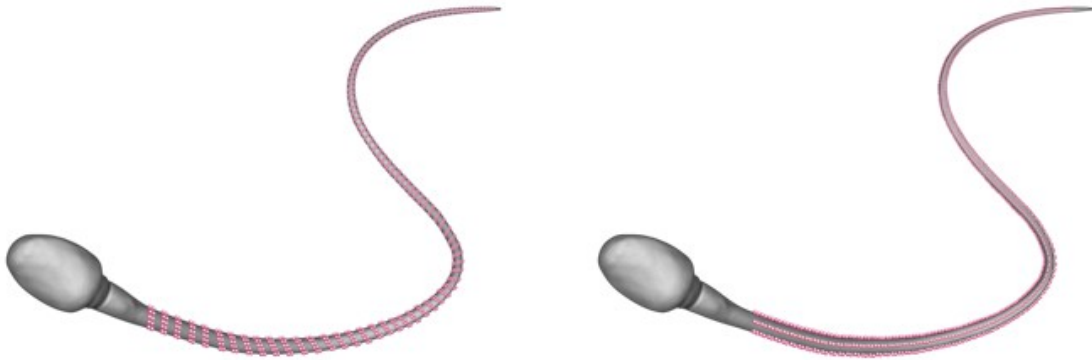


**Figure 29.** Two geometric models of the GC organization in a sperm flagellum. On the left, the model shows the helical organization of GCs (red) in an intact flagellum as determined in this work by cryo-electron tomography. On the right, the models show the “spaghetti” organization of GCs (red) used for simulation analysis. These two models are currently used to analyse the contribution of the GC architecture to the stiffness of the flagellum.

The rigidity of the flagellum is determined by several elements among which the axoneme might play the principal role. Depending on the rigidity contributed by the high density of GC rows, the GC architecture might significantly affect the overall bending stiffness of the flagellum. If the GC rows and the axoneme contribute to the overall stiffness in the same order of magnitude, then the GC organization might make a difference. The consequences of a helical or spaghetti organization are intuitively obvious on a qualitative level: it’s much easier to bend a helix or spring

even if the material it is made of is rigid; by contrast the spaghetti arrangement creates more resistance against flagellar motions. Simulation analyses are at the moment on-going to understand whether rigidity is the reason standing behind the helical GC architecture.

*Oligomeric state of GC.* The oligomeric state of membrane GC is a case of debate, and no structure is still not available for a full-length membrane GC. Biochemical assays including cross-linking techniques reveal dimers, trimers, tetramers or even larger multimers (Iwata *et al.* 1991; Chinker and Wilson 1992; Lowe 1992; Vandraager *et al.* 1994; Vijayachandra *et al.* 2000). More recently, single-particle EM images and X-rays structures of the extracellular ligand-binding domain of the mammalian GC-C show that it forms dimers (van den Akker *et al.* 2000; Ogawa *et al.* 2009). However, these studies were performed on isolated, solubilized protein samples; thus the oligomeric state of the full receptor in the native membrane is still unknown. Furthermore, biochemical assays might produce artefacts. For example, higher oligomers might reflect cross-linking artefacts due to changes in the protein conformation or in protein-protein contacts. A summary of different techniques and oligomeric state found for GC is reported on Table 2.

The cryo-ET data shown in this work are consistent with a dimeric state. The dimensions of an ECD dimer are similar to the ones reported by single-particle EM and X-ray crystallography (van den Akker *et al.* 2000; Ogawa *et al.* 2009). Moreover, the dimer is also consistent with previous work reporting the presence of a coiled-coil

domain that promotes dimer formation (Anantharaman *et al.* 2006; Saha *et al.* 2009) and with the GTP substrate-binding site formed at the interface of two monomers of a mammalian orthologue (Tucker *et al.* 1998). Finally, our data suggest that the dimer represents the functional unit in the native membrane at rest. This result will be further investigated to clarify the possible negative cooperativity among GC subunits, a mechanism that was hypothesized for the regulation of the binding affinity (Wachten *et al.* 2017).

Technique	Oligomeric state	Protein conditions	References
cross-linking	dimers and trimers	purified protein – heterologous expression	Lowe 1992
size exclusion chromatography	dimers, trimers, and tetramers	purified protein – enterotoxin from <i>E. coli</i>	Vandraager <i>et al.</i> 1994; Vijayachandra <i>et al.</i> 2000
immunoprecipitation	monomers and trimers	purified protein – heterologous expression	Chinker and Wilson 1992
affinity labelling	dimers	purified protein – bovine adrenal glands	Iwata <i>et al.</i> 1991;
X-ray crystallography	dimers	purified protein – heterologous expression	van den Akker <i>et al.</i> 2000
single-particle EM	dimers	purified protein – heterologous expression	Ogawa <i>et al.</i> 2009
cryo-electron tomography	dimers	protein under native conditions- in situ analysis	Our data

**Table 2:** Summary of different techniques applied to study GC oligomeric state. The table indicates the techniques used with the relative oligomeric state of GC. The protein conditions during the analysis of the oligomeric state are also indicated; in particular it is specified whether the analysis are made for proteins close-to-native conditions and *in situ*, or for purified proteins either from native tissue or heterologous expression.

## Literature

Al-Amoudi, A., Studer, D., Dubochet, J. (2005). Cutting artefacts and cutting process in vitreous sections for cryo-electron microscopy. *J Struct Biol.* 150, 109-21.

Al-Amoudi, A., Diez, D. C., Betts, M. J. Frangakis, A. S. (2007). The molecular architecture of cadherins in native epidermal desmosomes. *Nature.* 450, 832-838.

Allerston, C.K., von Delft, F., Gileadi, O. (2013). Crystal structures of the catalytic domain of human soluble guanylate cyclase. *PLoS One.* 8, e57644.

Alvarez, L., Friedrich, B.M., Gompper, G., Kaupp, U.B. (2014). The computational sperm cell. *Trends Cell Biol.* 24, 198-207.

Alvarez, L., Dai, L., Friedrich, B. M., Kashikar, N.D., Gregor, I., Pascal, R. , Kaupp, U.B. (2012). The rate of change in  $Ca^{2+}$  concentration controls sperm chemotaxis. *J. Cell Biol.* 196, 653-663.

Anantharaman, V., Balaji, S., Aravind, L. (2006). The signaling helix: a common functional theme in diverse signaling proteins. *Biol Direct.* 1, 25.

Armitage, J.P. (1992a). Behavioral responses in bacteria. *Annu Rev Physiol.* 54, 683-

714.

Armitage, J.P. (1992b). Bacterial motility and chemotaxis. *Sci Prog.* 76, 451-77.

Asano, A., Nelson, J.L., Zhang, S., Travis, A.J. (2010). Characterization of the proteomes associating with three distinct membrane raft sub-types in murine sperm. *Proteomics*.10, 3494–3505.

Bahat, A., Tur-Kaspa, I., Gakamsky, A., Giojalas, L.C., Breitbart, H., Eisenbach, M. (2003). Thermotaxis of mammalian sperm cells: A potential navigation mechanism in the female genital tract. *Nat Med.* 9, 149-50.

Bai, X.C., McMullan, G., Scheres, S.H. (2015). How cryo-EM is revolutionizing structural biology. *Trends Biochem Sci.* 40, 49-57.

Bharat, T.A., Scheres, S.H. (2016). Resolving macromolecular structures from electron cryo-tomography data using subtomogram averaging in RELION. *Nat Protoc.* 11, 2054-65.

Berg, H.C., Purcell, E.M. (1977). Physics of chemoreception. *Biophys. J.* 20, 193-219.

Berg, H.C., Brown, D.A. (1972). Chemotaxis in *Escherichia coli* analysed by three-

dimensional tracking. Nature. 239, 500-4.

Böhmer, M., Van, Q., Weyand, I., Hagen, V., Beyermann, M., Matsumoto, M., Hoshi, M., Hildebrand, E., Kaupp, U.B. (2005). Ca<sup>2+</sup> spikes in the flagellum control chemotactic behavior of sperm. EMBO J. 24, 2741-52.

Bönigk, W., Loogen, A., Seifert, R., Kashikar, N., Klemm, C., Krause, E., Hagen, V., Kremmer, E., Strunker, T., Kaupp, U.B. (2009). An atypical CNG channel activated by a single cGMP molecule controls sperm chemotaxis. Sci. Signal. 2, ra68.

Bostina, M., Bubeck, D., Schwartz, C., Nicastro, D., Filman, D.J., Hogle, J.M. (2007). Single particle cryoelectron tomography characterization of the structure and structural variability of poliovirus-receptor-membrane complex at 30 Å resolution. J Struct Biol. 160, 200-10.

Bray, D., Levin, M.D., Morton-Firth, C.J. (1998). Receptor clustering as a cellular mechanism to control sensitivity. Nature. 393, 85-8.

Brennan, P.A., Zufall, F. (2006). Pheromonal communication in vertebrates. Nature. 444, 308-15.

Briegel, A., Ding, H.J., Li, Z., Werner, J., Gitai, Z., Dias, D.P., Jensen, R.B., Jensen, G.J. (2008). Location and architecture of the *Caulobacter crescentus* chemoreceptor

array. *Mol Microbiol.* 69, 30-41.

Briegel, A., Wong, M.L., Hodges, H.L., Oikonomou, C.M., Piasta, K.N., Harris, M.J., Fowler, D.J., Thompson, L.K., Falke, J.J., Kiessling, L.L., Jensen, G.J. (2014). New insights into bacterial chemoreceptor array structure and assembly from electron cryotomography. *Biochemistry.* 53, 6624.

Burnett, A., Gomez, I., De Leon, D.D., Ariaans, M., Progias, P., Kammerer, R.A., Velasco, G., Marron, M., Hellewell, P., Ridger, V. (2017). Angiopoietin-1 enhances neutrophil chemotaxis in vitro and migration in vivo through interaction with CD18 and release of CCL4. *Sci Rep.* 7, 2332.

Burnett, L.A., Anderson, D.M., Rawls, A., Bieber, A.L., Chandler, D.E. (2011). Mouse sperm exhibit chemotaxis to allurin, a truncated member of the cysteine-rich secretory protein family. *Dev Biol.* 360, 318-28

Cannistraro, V.J., Glekas, G.D., Rao, C.V., Ordal, G.W. (2011). Cellular stoichiometry of the chemotaxis proteins in *Bacillus subtilis*. *J Bacteriol.* 193, 3220-7.

Chao, Y.C., Chen, C.C., Lin, Y.C., Breer, H., Fleischer, J., Yang, R.B. (2015). Receptor guanylyl cyclase-G is a novel thermosensory protein activated by cool temperatures. *EMBO J.* 34, 294-306.

Chao, Y.C., Cheng, C.J., Hsieh, H.T., Lin, C.C., Chen, C.C., Yang, R.B. (2010). Guanylate cyclase-G, expressed in the Grüneberg ganglion olfactory subsystem, is activated by bicarbonate. *Biochem J.* 432, 267-73.

Chen, N., Harris, T.W., Antoshechkin, I., Bastiani, C., Bieri, T., Blasiar, D., Bradnam, K., Canaran, P., Chan, J., Chen, C.K., Chen, W.J., Cunningham, F., Davis, P., Kenny, E., Kishore, R., Lawson, D., Lee, R., Muller, H.M., Nakamura, C., Pai, S., Ozersky, P., Petcherski, A., Rogers, A., Sabo, A., Schwarz, E.M., Van Auken, K., Wang, Q., Durbin, R., Spieth, J., Sternberg, P.W., Stein, L.D. (2005). WormBase: a comprehensive data resource for *Caenorhabditis* biology and genomics. *Nucleic Acids Res.* 33, D383-9.

Chinkers, M., Wilson, E.M. (1992). Ligand-independent oligomerization of natriuretic peptide receptors. Identification of heteromeric receptors and a dominant negative mutant. *J Biol Chem.* 267, 18589-97.

Chung, J.J., Shim, S.H., Everley, R.A., Gygi, S.P., Zhuang, X., Clapham, D.E. (2014). Structurally distinct Ca<sup>(2+)</sup> signaling domains of sperm flagella orchestrate tyrosine phosphorylation and motility. *Cell.* 157, 808-22.

Cope, J., Heumann, J., Hoenger, A. (2011). Cryo-electron tomography for structural characterization of macromolecular complexes. *Curr. Protoc. Protein Sci.* Chapter 17, Unit 17.

Corkidi, G., Taboada, B., Wood, C.D., Guerrero, A., Darszon, A. (2008). Tracking sperm in three-dimensions. *Biochem Biophys Res Commun.* 373, 125-9.

Dierksen, K., Typke, D., Hegerl, R., Baumeister, W. (1993). Towards automatic electron tomography. II. Implementation of autofocus and low-dose procedures. *Ultramicroscopy*, 49, 109-120.

Dizhoor, A.M., Hurley, J.B. (1999). Regulation of photoreceptor membrane guanylyl cyclases by guanylyl cyclase activator proteins. *Methods.* 19, 521-31.

Dizhoor, A.M., Olshevskaya, E.V., Henzel, W.J., Wong, S.C., Stults, J.T., Ankoudinova, I., Hurley, J.B. (1995). Cloning, sequencing, and expression of a 24-kDa  $\text{Ca}^{2+}$ -binding protein activating photoreceptor guanylyl cyclase. *J Biol Chem.* 270, 25200-6.

Dizhoor, A.M., Lowe, D.G., Olshevskaya, E.V., Laura, R.P., Hurley, J.B. (1994). The human photoreceptor membrane guanylyl cyclase, RetGC, is present in outer segments and is regulated by calcium and a soluble activator. *Neuron.* 12, 1345-52

Duke, T.A., Bray, D. (1999). Heightened sensitivity of a lattice of membrane receptors. *Proc Natl Acad Sci U S A.* 96, 10104-8.

Dusenbery, D.B. (1998). Spatial Sensing of Stimulus Gradients Can Be Superior to Temporal Sensing for Free-Swimming Bacteria. *Biophys J.* 74, 2272-7.

Dusenbery, D.B. (1992). *Sensory Ecology*. W. H. Freeman, New York.

Eddy, E.M., Toshimori, K., O'Brien, D.A. (2003). Fibrous sheath of mammalian spermatozoa. *Microsc Res Tech.* 61, 103-15. Review.

Egerton, R.F., Li, P., Malac, M. (2004). Radiation damage in the TEM and SEM. *Micron.* 35, 399-409.

Elgeti, J., Gompper, G., (2016). Microswimmers near surfaces. *Eur. Phys. J. Special Topics* 225, 3033.

Elgeti, J., Kaupp, U.B., Gompper, G. (2010). Hydrodynamics of sperm cells near surfaces. *Biophys J.* 99, 1018-26.

Endres, R.G., Wingreen, N.S. (2006). Precise adaptation in bacterial chemotaxis through "assistance neighborhoods". *Proc Natl Acad Sci U S A.* 103, 13040-4.

Förster, F., Medalia, O., Zauberman, N., Baumeister, W., Fass, D. (2005). Retrovirus envelope protein complex structure in situ studied by cryo-electron tomography. *Proc Natl Acad Sci U S A.* 102, 4729-34.

Fotiadis, D., Liang, Y., Filipek, S., Saperstein, D. A., Engel, A., Palczewski, K. (2003). Atomic-force microscopy: rhodopsin dimers in native disc membranes. *Nature*. 421, 127-128

Frank, J. (1992). *Electron tomography: three-dimensional imaging with the transmission electron microscope*. Plenum, New York 154. Lawrence MC.

Frank, J. (2006). *Three-dimensional electron microscopy of macromolecular assemblies: visualization of biological molecules in their native state*. Oxford University Press. Oxford.

Gauss, R., Seifert, R., Kaupp, U.B. (1998). Molecular identification of a hyperpolarization-activated channel in sea urchin sperm. *Nature*. 393, 583-7.

Gestwicki, J.E., Lamanna, A.C., Harshey, R.M., McCarter, L.L., Kiessling, L.L., Adler, J. (2000). Evolutionary conservation of methyl-accepting chemotaxis protein location in Bacteria and Archaea. *J Bacteriol*. 182, 6499-502.

Gestwicki, J.E., Kiessling, L.L. (2002). Inter-receptor communication through arrays of bacterial chemoreceptors. *Nature*. 415, 81-4.

Gilbert, P. (1972). Iterative methods for the three-dimensional reconstruction of an

object from projections. *J Theor Biol.* 36, 105-17.

Gorczyca, W.A., Gray-Keller, M.P., Detwiler, P.B., Palczewski, K. (1994). Purification and physiological evaluation of a guanylate cyclase activating protein from retinal rods. *Proc Natl Acad Sci USA.* 91, 4014-8.

Guerrero, A., Nishigaki, T., Carneiro, J., Yoshiro, T., Wood, C.D., Darszon, A. (2010). Tuning sperm chemotaxis by calcium burst timing. *Dev Biol.* 344, 52–65.

Gunaratne, H.J., Vacquier, V.D. (2006). Evidence for a secretory pathway  $\text{Ca}^{2+}$ -ATPase in sea urchin spermatozoa. *FEBS Lett.* 580, 3900-4.

Gundersen, R. (1985). Sensory neurite growth cone guidance by substrate adsorbed nerve growth factor. *J Neurosci Res.* Vol. 13, pp. 199-212.

Gunkel, M., Schöneberg, J., Alkhaldi, W., Irsen, S., Noé, F., Kaupp, U.B., Al-Amoudi, A. (2015). Higher-order architecture of rhodopsin in intact photoreceptors and its implication for phototransduction kinetics. *Structure.* 23, 628-38.

Guo, W., Chen, H. (2012). Improving SIRT Algorithm for Computerized Tomographic Image Reconstruction. Chapter, *Recent Advances in Computer Science and Information Engineering.* Volume 128 of the series *Lecture Notes in Electrical Engineering*, pp 523-528.

Hall, S.R. (1991). The STAR file: a new format for electronic data transfer and archiving. *J Chem Inform Comp Sci.* 31, 326-33.

Hamra, F.K., Forte, L.R., Eber, S.L., Pidhorodeckyj, N.V., Krause, W.J., Freeman, R.H., Chin, D.T., Tompkins, J.A., Fok, K.F., Smith, C.E., Duffin, K.L., Siegel, N.R., Currie, M.G. (1993). Uroguanylin: structure and activity of a second endogenous peptide that stimulates intestinal guanylate cyclase. *Proc Natl Acad Sci U S A.* 90, 10464-8.

Han, L., Monné, M., Okumura, H., Schwend, T., Cherry, A.L., Flot, D., Matsuda, T., Jovine, L. (2010). Insights into egg coat assembly and egg-sperm interaction from the X-ray structure of full-length ZP3. *Cell.* 143, 404-15.

Hansbrough, J.R., Garbers, D.L. (1981). Speract. Purification and characterization of a peptide associated with eggs that activates spermatozoa. *J Biol Chem.* 256, 1447-52.

Hayat, M.A., Miller, S.E. (1990). *Negative staining.* McGraw-Hill, New York.

Hazelbauer, G.L., Falke, J.J., Parkinson, J.S. (2008). Bacterial chemoreceptors: high-performance signaling in networked arrays. *Trends Biochem Sci.* 33, 9-19.

Hazelbauer, G.L. (1988). The bacterial chemosensory system. *Can. J. Microbiol.* 34,

466-74.

Heuser, T., Raytchev, M., Krell, J., Porter, M.E., Nicastro, D. (2009). The dynein regulatory complex is the nexin link and a major regulatory node in cilia and flagella. *J Cell Biol.* 187, 921-33.

Heymann, J.B., Butan, C., Winkler, D.C., Craven, R.C., Steven, A.C. (2008). Irregular and Semi-Regular Polyhedral Models for Rous Sarcoma Virus Cores. *Comput Math Methods Med.* 9, 197-210.

Hille, B. (2001). *Ionic Channels of Excitable Membranes*. Third edition. Sinauer Associates, Sunderland, MA. 814 pp.

Hugh, C. (1911). Chemotaxis. *Encycloaedia Britannica*. Vol. 6, p. 77. Cambridge Univeristy Press.

Iglesias, P.A. (2012). A systems biology view of adaptation in sensory mechanisms. *Adv. Exp Med Biol.* 736, 499-516.

Iwata, T., Uchida-Mizuno, K., Katafuchi, T., Ito, T., Hagiwara, H., Hirose, S. (1991). Bifunctional atrial natriuretic peptide receptor (type A) exists as a disulfide-linked tetramer in plasma membranes of bovine adrenal cortex. *J Biochem.* 110, 35-9.

Jikeli, J.F., Alvarez, L., Friedrich, B.M., Wilson, L.G., Pascal, R., Colin, R., Pichlo, M., Rennhack, A., Brenker, C., Kaupp, U.B. (2015). Sperm navigation along helical paths in 3D chemoattractant landscapes. *Nat Commun.* 6, 7985.

Kashikar, N.D., Alvarez, L., Seifert, R., Gregor, I., Jäckle, O., Beyermann, M., Krause, E., Kaupp, U.B. (2012). Temporal sampling, resetting, and adaptation orchestrate gradient sensing in sperm. *J Cell Biol.* 198, 1075-91.

Kaupp, U.B., Strünker, T. (2017). Signaling in Sperm: More Different than Similar. *Trends Cell Biol.* 27, 101-9.

Kaupp, U.B., Alvarez, L. (2016). Sperm as microswimmers – navigation and sensing at the physical limit. *Eur Phys J Spec Top.* 225, 2119-39.

Kaupp, U.B. (2012). 100 years of sperm chemotaxis. *J Gen Physiol.* 140, 583-6.

Kaupp, U.B., Kashikar, N.D., Weyand, I. (2008). Mechanisms of sperm chemotaxis. *Annu. Rev. Physiol.* 70, 93-117.

Kaupp, U.B., Solzin, J., Hildebrand, E., Brown, J. E., Helbig, A., Hagen, V., Beyermann, M., Pampaloni, F., Weyand, I. (2003). The signal flow and motor response controlling chemotaxis of sea urchin sperm. *Nat. Cell. Biol.* 5, 109-117.

Kilic, F., Kashikar, N.D., Schmidt, R., Alvarez, L., Dai, L., Weyand, I., Wiesner, B., Goodwin, N., Hagen, V., Kaupp, U.B. (2009). Caged progesterone: a new tool for studying rapid nongenomic actions of progesterone. *J Am Chem Soc.* 131, 4027-30.

Kilic, O., Pamies, D., Lavell, E., Schiapparelli, P., Feng, Y., Hartung, T., Bal-Price, A., Hogberg, H.T., Quinones-Hinojosa, A., Guerrero-Cazares, H., Levchenko, A. (2016). Brain-on-a-chip model enables analysis of human neuronal differentiation and chemotaxis. *Lab Chip.* 16, 4152-62.

Knobil, E., Neill, J.D. (2015). *Physiology of Reproduction.* (4th edn), Elsevier.

Koller, K.J., de Sauvage, F.J., Lowe, D.G., Goeddel, D.V. (1991). Conservation of the kinase like regulatory domain is essential for activation of the natriuretic peptide receptor guanylyl cyclases. *Mol Cell Biol.* 12, 2581-90.

Kopf, G.S. (2002). Signal transduction mechanisms regulating sperm acrosomal exocytosis. *Fertilization*, Chapter 6, pp. 181-223. Academic Press. Elsevier Inc.

Kuhn, M. (2003). Structure, regulation, and function of mammalian membrane guanylyl cyclase receptors, with a focus on guanylyl cyclase-A. *Circ Res.* 93, 700-9.

Li, G., Weis R.M. (2000). Covalent modification regulates ligand binding to receptor complexes in the chemosensory system of *Escherichia coli*. *Cell.* 100, 357-65.

Li, M., Hazelbauer, G.L. (2004). Cellular stoichiometry of the components of the chemotaxis signaling complex. *J Bacteriol.* 186, 3687-94.

Li, M., Hazelbauer, G.L. (2005). Adaptational assistance in clusters of bacterial chemoreceptors. *Mol Microbiol.* 56, 1617-26.

Lindemann, C.B., Goltz, J.S. (1988). Calcium regulation of flagellar curvature and swimming pattern in triton X-100-extracted rat sperm. *Cell Motil Cytoskeleton.* 10, 420-31.

Lindemann, C.B. (1996). Functional significance of the outer dense fibers of mammalian sperm examined by computer simulations with the geometric clutch model. *Cell Motil Cytoskeleton.* 34, 258-70.

Lindemann, C.B., Gardner, T.K., Westbrook, E., Kanous, K.S. (1991). The calcium-induced curvature reversal of rat sperm is potentiated by cAMP and inhibited by anti-calmodulin. *Cell Motil Cytoskeleton.* 20, 316-24.

Loos, J., Sourty, E., Lu, K., Freitag, B., Tang, D., Wall, D. (2009). Electron tomography on micrometer-thick specimens with nanometer resolution. *Nano Letters.* 9, 1704-1708.

Lowe, D.G. (1992). Human natriuretic peptide receptor-A guanylyl cyclase is self-associated prior to hormone binding. *Biochemistry*. 31, 10421-5.

Mastronarde, D.N. (1997). Dual-axis tomography: an approach with alignment methods that preserve resolution. *J. Struct. Biol.* 120, 343-352.

Mastronarde, D.N. (2005). Automated electron microscope tomography using robust prediction of specimen movements. *J Struct Biol.* 152, 36-51.

Matsumoto, M., Solzin, J., Helbig, A., Hagen, V., Ueno, S.I., Kawase, O., Maruyama, Y., Ogiso, M., Godde, M., Minakata, H., Kaupp, U.B., Hoshi, M., Weyand, I. (2003). A sperm-activating peptide controls a cGMP signaling pathway in starfish sperm. *Dev Biol.* 260: 314-24.

McIntosh, R., Nicastro, D., Mastronarde, D. (2005). New views of cells in 3D: an introduction to electron tomography. *Trends Cell Biol.* 15, 43-51.

Meyer, M.R., Angele, A., Kremmer, E., Kaupp, U.B., Muller, F. (2000). A cGMP-signaling pathway in a subset of olfactory sensory neurons. *Proc Natl Acad Sci U S A.* 97, 10595-600.

Miki, K., Clapham, D.E. (2013). Rheotaxis guides mammalian sperm. *Curr. Biol.* 23, 443-52.

Milne, J.L.S., Borgnia, M.J., Bartesaghi, A., Tran, E.E.H., Earl, L.A., Schauder, D.M., Lengyel, J., Pierson, J., Patwardhan, A., Subramaniam, S. (2013). Cryo-electron microscopy: A primer for the non-microscopist. *FEBS J.* 280, 28-45.

Murray, M.J. (2017). The role of netrins and their receptors in epithelial mesenchymal plasticity during development. *Cells Tissues Organs.* 203, 71-81.

Nicastro, D., Schwartz, C., Pierson, J., Gaudette, R., Porter, M.E., McIntosh, J.R. (2006). The molecular architecture of axonemes revealed by cryoelectron tomography. *Science.* 313, 944-8.

Nicastro, D. (2009). Cryo-electron microscope tomography to study axonemal organization. *Methods Cell Biol.* 91, 1-39.

Nickell, S., Forster, F., Linaroudis, A., Net, W.D., Beck, F., Hegerl, R., Baumeister, W., Plitzko, J.M. (2005). TOM software toolbox: acquisition and analysis for electron tomography *J Struct Biol.* 149, 227-34.

Nishigaki, T., Darszon, A. (2000). Real-time measurements of the interactions between fluorescent speract and its sperm receptor. *Dev Biol.* 223, 17-26.

Nishigaki, T., Chiba, K., Miki, W., Hoshi, M. (1996). Structure and function of

asterosaps, sperm-activating peptides from the jelly coat of starfish eggs. *Zygote*. 4, 237-45.

Ogawa, H., Qiu, Y., Huang, L., Tam-Chang, S.W., Young, H.S., Misono, K.S. (2009). Structure of the atrial natriuretic peptide receptor extracellular domain in the unbound and hormone-bound states by single-particle electron microscopy. *FEBS J*. 276, 1347-55.

Olson, J.H., Xiang, X., Ziegert, T., Kittelson, A., Rawls, A., Bieber, A.L., Chandler, D.E. (2001). Allurin, a 21-kDa sperm chemoattractant from *Xenopus* egg jelly, is related to mammalian sperm-binding proteins. *Proc Natl Acad Sci USA*. 98, 11205-10.

Palczewski, K., Subbaraya, I., Gorczyca, W.A., Helekar, B.S., Ruiz, C.C., Ohguro, H., Huang, J., Zhao, X., Crabb, J.W., Johnson, R.S., Walsh, K.A., Gray-Keller, M.P., Detwiler, P.B., Baehr, W. (1994). Molecular cloning and characterization of retinal photoreceptor guanylyl cyclase-activating protein. *Neuron*. 13, 395-404.

Penczek, P., Marko, M., Buttle, K., Frank, J. (1995). Double-tilt electron tomography. *Ultramicroscopy*. 60, 393-410.

Pettersen, E.F., Goddard, T.D., Huang, C.C., Couch, G.S., Greenblatt, D.M., Meng, E.C., Ferrin, T.E. (2004). UCSF Chimera--a visualization system for exploratory

research and analysis. *J Comput Chem.* 25, 1605-12.

Pichlo, M., Bungert-Plümke, S., Weyand, I., Seifert, R., Bönigk, W., Strünker, T., Kashikar, N.D., Goodwin, N., Müller, A., Körschen, H.G., Collienne, U., Pelzer, P., Van, Q., Enderlein, J., Klemm, C., Krause, E., Trötschel, C., Poetsch, A., Kremmer, E., Kaupp, U.B. (2014). High density and ligand affinity confer ultrasensitive signal detection by a guanylyl cyclase chemoreceptor. *J Cell Biol.* 207, 675.

Potter, L.R. (2011). Guanylyl cyclase structure, function and regulation. *Cell Sign.* 23, 1921-6.

Ramot D, MacInnis BL, Goodman MB. (2008). Bidirectional temperature-sensing by a single thermosensory neuron in *C. Elegans*. *Nat Neurosci.* 11, 908-15.

Rath, B.K., Marko, M., Radermacher, M., Frank, J. (1997). Low-dose automated electron tomography: a recent implementation *J Struct Biol.* 120, 210-8.

Rauch, A., Leipelt, M., Russwurm, M., Steegborn, C. (2008a). Crystal structure of the guanylyl cyclase Cya2. *Proc. Natl. Acad. Sci. USA.* 105, 15720-15725.

Rauch, A., Leipelt, M., Russwurm, M. and Steegborn, C. (2008b). Crystal structure of the guanylyl cyclase Cya2. *Proc. Natl. Acad. Sci. USA* 105, 15720-15725.

Riffell, J.A., Zimmer, R.K. (2007). Sex and flow: the consequences of fluid shear for sperm-egg interactions. *J Exp Biol.* 210, 3644-60.

Romanova, E.A., Dukhanina, E.A., Sharapova, T.N., Sashchenko, L.P., Gnuchev, N.V., Yashin, D.V. (2017). Lymphocytes incubated in the presence of IL-2 lose the capacity for chemotaxis but acquire antitumor activity. *Dokl Biol Sci.* 472, 31-3.

Saha, S., Biswas, K.H., Kondapalli, C., Isloor, N., Visweswariah, S.S. (2009). The linker region in receptor guanylyl cyclases is a key regulatory module: mutational analysis of guanylyl cyclase C. *J Biol Chem.* 284, 27135-45.

Scheres, S.H. (2012). RELION: implementation of a Bayesian approach to cryo-EM structure determination. *J Struct Biol.* 180, 519-30.

Schertler, G.F. (2015). Rhodopsin on tracks: new ways to go in signaling. *Structure.* 23, 606-8.

Schmid, M.F., Booth, C.R. (2008). Methods for aligning and for averaging 3D volumes with missing data. *J Struct Biol.* 161, 243-8.

Seifert, R., Flick, M., Bönigk, W., Alvarez, L., Trötschel, C., Poetsch, A., Müller, A., Goodwin, N., Pelzer, P., Kashikar, N.D., Kremmer, E., Jikeli, J., Timmermann, B., Kuhl, H., Fridman, D., Windler, F., Kaupp, U.B., Strünker, T. (2015). The CatSper

channel controls chemosensation in sea urchin sperm. *EMBO J.* 34, 379-92.

Shimomura, H., Dangott, L.J., Garbers, D.L. (1986). Covalent coupling of a resact analogue to guanylate cyclase. *J Biol Chem.* 261, 15778-82.

Singh, S., Lowe, D.G., Thorpe, D.S., Rodriguez, H., Kuang, W.J., Dangott, L.J., Chinkers, M., Goeddel, D.V., Garbers, D.L. (1988). Membrane guanylate cyclase is a cell-surface receptor with homology to protein kinases. *Nature.* 334, 708-12.

Sourjik, V., Berg, H.C. (2002). Receptor sensitivity in bacterial chemotaxis. *Proc Natl Acad Sci USA.* 99,123–127

Sourjik, V., Berg, H.C. (2004). Functional interactions between receptors in bacterial chemotaxis. *Nature.* 428, 437-41.

Sourjik, V., Armitage, J.P. (2010). Spatial organization in bacterial chemotaxis. *EMBO J.* 29, 2724-33.

Sourjik, V., Wingreen, N.S. (2012). Responding to chemical gradients: bacterial chemotaxis. *Curr Opin Cell Biol.* 24, 262-8.

Strünker, T., Weyand, I., Bonigk, W., Van, Q., Loogen, A., Brown, J. E., Kashikar, N., Hagen, V., Krause, E. and Kaupp, U. B. (2006). A K<sup>+</sup>-selective cGMP-gated ion

channel controls chemosensation of sperm. *Nat. Cell. Biol.* 8, 1149-1154.

Su, Y.H., Vacquier, V.D. (2006). Cyclic GMP-specific phosphodiesterase-5 regulates motility of sea urchin spermatozoa. *Mol Biol Cell.* 17, 114-21.

Su, Y.H., Vacquier, V.D. (2002). A flagellar K(+)-dependent Na(+)/Ca(2+) exchanger keeps Ca(2+) low in sea urchin spermatozoa. *Proc Natl Acad Sci U S A.* 99, 6743-8.

Suarez, S.S., Pacey, A.A. (2006). Sperm transport in the female reproductive tract. *Hum. Reprod.* 12, 23–37.

Suga, S., Nakao, K., Hosoda, K., Mukoyama, M., Ogawa, Y., Shirakami, G., Arai, H., Saito, Y., Kambayashi, Y., Inouye, K., Imura, H. (1992). Receptor selectivity of natriuretic peptide family, atrial natriuretic peptide, brain natriuretic peptide, and C-type natriuretic peptide. *Endocrinology.* 130, 229-39.

Suzuki, N., Garbers, D.L. (1984). Stimulation of sperm respiration rates by speract and resact at alkaline extracellular pH. *Biol. Reprod.* 30, 1167-1174.

Suzuki, N., Shimomura, H., Radany, E. W., Ramarao, C. S., Ward, G. E., Bentley, J. K. and Garbers, D. L. (1984). A peptide associated with eggs causes a mobility shift in a major plasma membrane protein of spermatozoa. *J. Biol. Chem.* 259, 14874-14879.

Swaney, K.F., Huang, C.H., Devreotes, P.N. (2010). Eukaryotic Chemotaxis: A Network of Signaling Pathways Controls Motility, Directional Sensing, and Polarity. *Annu Rev Biophys.* 39, 265-89.

Takeishi, A., Yu, Y.V., Hapiak, V.M., Bell, H.W., O'Leary, T., Sengupta, P. (2016). Receptor-type guanylyl cyclases confer thermosensory responses in *C. elegans*. *Neuron.* 90, 235-44.

Thorpe, D.S., Niu, S., Morkin, E. (1991). Overexpression of dimeric guanylyl cyclase cores of an atrial natriuretic peptide receptor. *Biochem. Biophys. Res. Commun.* 180, 538-44.

Tucker, C.L., Hurley, J.H., Miller, T.R., Hurley, J.B. (1998). Two amino acid substitutions convert a guanylyl cyclase, RetGC-1, into an adenylyl cyclase. *Proc Natl Acad Sci U S A.* 95, 5993-7.

van den Akker, F., Zhang, X., Miyagi, M., Huo, X., Misono, K. S., Yee, V. C. (2000). Structure of the dimerized hormone-binding domain of a guanylyl-cyclase-coupled receptor. *Nature.* 406, 101-104.

Vaandrager, A.B., van der Wiel, E., Hom, M.L., Luthjens, L.H., de Jonge, H.R. (1994). Heat-stable enterotoxin receptor/guanylyl cyclase C is an oligomer consisting of functionally distinct subunits, which are non-covalently linked in the intestine. *J*

Biol Chem. 269, 16409-15.

Venkatesh, M.J., Subramaniam S. (2013). Chemoreceptor arrays. Encyclopedia of Biophysics. Gordon GKC, ed. Springer (NY), pp. 293-296.

Vidal-Gadea, A., Ward, K., Beron, C., Ghorashian, N., Gokce, S., Russell, J., Truong, N., Parikh, A., Gadea, O., Ben-Yakar, A., Pierce-Shimomura, J. (2015). Magnetosensitive neurons mediate geomagnetic orientation in *Caenorhabditis elegans*. *Elife*. 4, e07493.

Vijayachandra, K., Guruprasad, M., Bhandari, R., Manjunath, U.H., Somesh, B.P., Srinivasan, N., Suguna, K., Visweswariah, S.S. (2000). Biochemical characterization of the intracellular domain of the human guanylyl cyclase C receptor provides evidence for a catalytically active homotrimer. *Biochemistry*. 39, 16075-83.

Wachten, D., Jikeli, J.F., Kaupp, U.B. (2017). Sperm Sensory Signaling. *Cold Spring Harb Perspect Biol*. pii: a028225.

Ward, G.E., Brokaw, C.J., Garbers, D.L., Vacquier, V.D. (1985). Chemotaxis of *Arbacia punctulata* spermatozoa to resact, a peptide from the egg jelly layer. *J Cell Biol*. 101, 2324-9.

Wilson, E.M., Chinkers, M. (1995). Identification of sequences mediating guanylyl

cyclase dimerization. *Biochemistry*. 34, 4696-701.

Winger, J.A., Derbyshire, E.R., Lamers, M.H., Marletta, M.A., Kuriyan, J. (2008). The crystal structure of the catalytic domain of a eukaryotic guanylate cyclase. *BMC Struct Biol*. 8, 42.

Wiseman, D.M., Polverini, P.J., D. Kamp, W., Leibovich, S.J. (1988). Transforming growth factor-beta (tgf) is chemotactic for human monocytes and induces their expression of angiogenic activity," *Biochem Biophys Res Com*. Vol. 157, pp. 793-800.

Wood, C.D., Nishigaki, T., Furuta, T., Baba, S.A., Darszon, A. (2005). Real-time analysis of the role of Ca<sup>2+</sup> in flagellar movement and motility in single sea urchin sperm. *J Cell Biol*. 169, 725-31.

Yasoda, A., Ogawa, Y., Suda, M., Tamura, N., Mori, K., Sakuma, Y., Chusho, H., Shiota, K., Tanaka, K. and Nakao, K. (1998). Natriuretic peptide regulation of endochondral ossification. Evidence for possible roles of the C-type natriuretic peptide/guanylyl cyclase-B pathway. *J. Biol. Chem*. 273, 11695-11700.

Zhang, J., Pacifico, R., Cawley, D., Feinstein, P., Bozza, T. (2013). Ultrasensitive detection of amines by a trace amine-associated receptor. *J Neurosci*. 33, 3228-39.

Zheng, S.Q., Keszthelyi, B., Branlund, E., Lyle, J.M., Braunfeld, M.B., Sedat, J.W., Agard, D.A. (2007). UCSF tomography: an integrated software suite for real-time electron microscopic tomographic data collection, alignment, and reconstruction. *J Struct Biol.* 157, 138-47.

Zheng, Q.S., Braunfeld, M.B., Sedat, J.W., Agard, D.A. (2004). An improved strategy for automated electron microscopic tomography. *J Struct Biol.* 147, 91-101.

Ziese, U., Geerts, W.J., Van Der Krift, T.P., Verkleij, A.J., Koster, A.J. (2003). Correction of autofocusing errors due to specimen tilt for automated electron tomography. *J Microsc.* 211, 179-85.

Ziese, U., Janssen, A.H., Murk, J.L., Geerts, W.J., Van der Krift, T.P., Verkleij, A.J., Koster A.J. (2002). Automated high-throughput electron tomography by pre-calibration of image shifts. *J Microsc.* 205, 187-200.

## **Acknowledgements**

The present study was developed in the Department of Molecular Sensory Systems at the Research Center caesar in Bonn (Germany). I would like to thank all the staff for their support and cooperation. My special thanks are especially for:

Prof. Dr. U.B. Kaupp for assigning me the project and for the many scientific discussions about it. I thank him for the great support during the whole PhD program, and especially for the patience in teaching me how to perform a scientific writing; Dr. S. Irsen for being always present and teaching me all about electron microscopy, but also for the great work done on the microscope itself to allow me to have the best set-up for the acquisition of the data set in this project; Dr. A. Al-Amoudi for bringing me close to cryo-electron tomography and sub-tomogram averaging; Dr. Elmar Behrmann for kindly revising the thesis, and for his support with the data evaluation and processing; the all EMA team, in particular C. Tröger, D. Rudolph and C. Bitdinger, for instruction in devices, sample preparation techniques and help with technical and computer-related problems; C. Bernsdorff and R. Pascal for the support during the preparation of 3D images of the GC model; and last but not least Mrs. H. Krause for her friendly help with all administrative and organizational tasks.

I would like to thank Prof. Dr. G. Schwarz (Universität Köln - Germany) for accepting to be supervisors of my PhD thesis and for evaluating it.

A kind thank also goes to Prof. Dr. S. I. Korsching (Universität Köln - Germany) and Dr. Stephan Irsen for accepting to be part of my PhD committee.

I would like to thank all the colleagues from CAESAR and DZNE, especially my dearest friends Zhiyang and Gayathri for the support, the discussions and the funny moments spent together during these years.

Lots of thanks go also to my former colleagues from the Università degli Studi di Cagliari, Davide and Gabriella for the nice time spent together in Frankfurt, Berlin, and Grenoble. A special thank goes to Dr. Dario Piano from the Università degli Studi di Cagliari, for being the one who gave me the start into the scientific world, giving me the tools to understand systems that are “out of the box”, for the useful scientific discussions, and for always being on my side also as a good friend.

Finally, my very special thanks go to my parents, my brothers and sister that always supported me and gave me all they could to let me feeling loved and to be present even from far away.

## **Erklärung**

Ich versichere, daß ich die von mir vorgelegte Dissertation selbständig angefertigt, die benutzten Quellen und Hilfsmittel vollständig angegeben und die Stellen der Arbeit – einschließlich Tabellen, Karten und Abbildungen –, die anderen Werken im Wortlaut oder dem Sinn nach entnommen sind, in

jedem Einzelfall als Entlehnung kenntlich gemacht habe; daß diese Dissertation noch keiner anderen Fakultät oder Universität zur Prüfung vorgelegen hat; daß sie – abgesehen von unten angegebenen Teilpublikationen – noch nicht veröffentlicht worden ist sowie, daß ich eine solche Veröffentlichung vor Abschluß des Promotionsverfahrens nicht vornehmen werde. Die Bestimmungen dieser Promotionsordnung sind mir bekannt. Die von mir vorgelegte Dissertation ist von Prof. Dr. U. B. Kaupp betreut worden.

Köln, 17/07/2017

sign here

## **Teilpublikationen**

**Farci D**, Irsen S, Al-Amoudi A, Behrmann E, Kaupp UB. Spatial organization of a chemoreceptor guanylate cyclase in the flagellum of *Arbacia punctulata* sperm. (manuscript in preparation).

## **Weitere Publikationen**

Collu G, **Farci D**, Esposito F, Pintus F, Kirkpatrick J, Piano D. *New insights into the operative network of FaEO, an enone oxidoreductase from Fragaria x ananassa Duch.* Plant Mol Biol, **2017**, doi:10.1007/s11103-017-0597-5.

**Farci D**, Esposito F, El Alaoui S, Piano D. *S-layer proteins as a source of carotenoids: isolation of the protein cofactor deinoxanthin from its S-layer protein DR\_2577.* Food Res Intern, **2016**, doi: 10.1016/j.foodres.2016.10.003.

**Farci D**, Kirkpatrick J, Piano D. *A new procedure for a fast soft staining of BN-PAGEs on photosynthetic complexes.* Electrophoresis, **2016**, doi: 10.1002/elps.201600389.

**Farci D**, Collu G, Kirkpatrick J, Esposito F, Piano D. *RhVII is a membrane-anchored vacuolar invertase highly expressed in Rosa hybrida L. petals.* J Exp Bot. **2016**, doi: 10.1093/jxb/erw148.

**Farci D**, Slavov C, Tramontano E, Piano D. *The S-layer protein DR\_2577 binds the carotenoid deinoxanthin and under desiccation conditions protect against UV-radiation in Deinococcus radiodurans.* Frontiers in Microbiology, section of Extreme Microbiology, research topic Photobiology of Extremophiles, **2016**, doi:10.3389/fmicb.2016.00155.

Haniewicz P, Floris D, **Farci D**, Kirkpatrick J, Loi MC, Büchel C, Bochtler M, Piano D. *Isolation of plant Photosystem II complexes by fractional solubilisation*. *Frontiers in Plant Sciences*, Plant Cell Biology journal, research topic Assembly of the Photosystem II Membrane-Protein Complex of Oxygenic Photosynthesis, **2015**, doi: 10.3389/fpls.2015.01100.

**Farci D**, Bowler MW, Esposito F, McSweeney S, Tramontano E, Piano D. *Purification and characterization of DR\_2577 (SlpA) a major S-layer protein from Deinococcus radiodurans*. *Frontiers in Microbiology*, **2015**, doi:10.3389/fmicb.2015.00414.

**Farci D**, Bowler MW, Kirkpatrick J, McSweeney S, Tramontano E, Piano D. *New features of the cell wall of the radio-resistant bacterium Deinococcus radiodurans*. *Biochim Biophys Acta*, **2014**, doi:10.1016/j.bbamem.2014.02.014.

## Curriculum Vitae

### Personal information

First name / Surname   Domenica Farci  
Address           Ludwig-Erhard-Allee 2, 53175, Bonn (Germany)  
Mobile           00393391492030  
E-mail           domenica.farci@caesar.de ; farcidomenica@live.it  
Nationality       Italian  
Date of birth      24/02/1990  
Gender            Female

### Education and training

Dates	01/08/2014 – present
Principal subject	Cryo-electron microscopy studies of chemoreceptors array on cells
skills covered	Cryo-Electron Tomography, Image Processing and 3D reconstruction
Name and type of organisation providing education and training	Center of Advanced European Studies and Research (CAESAR) – Associated Institute of the Max Planck Society; Department of Molecular Sensory System; Laboratory of Electron Microscopy. Referents: Prof. Dr. Ulrich Benjamin Kaupp; Dr. Elmar Behrmann; Dr. Stephan Irsen; Dr. Ashraf Al-Amoudi
Level in nation or international classification	PhD degree in Biochemistry, University of Cologne, Germany (thesis dissertation will be held on October 2017)
<hr/>	
Dates	01/09/2015 – 11/09/15
Title of qualification awarded	Intensive post-graduate level module of lectures and instruction (58h)
Skills covered	Image Processing for Cryo-electron microscopy
Name and type of organisation providing education and training	EMBO, Birkbeck University (London). Referents: Prof. Elena Orlova; Prof. Helen Saibil
<hr/>	
Dates	05/12/2014
Title of qualification awarded	FELASA B certificate, for laboratory animal science
Name and type of organisation providing education and training	Proবাদis Partner für Bildung und Beratung, Frankfurt am Main, Germany

<hr/>	
Dates	18/09/2012 – 23/07/2014
Title of qualification awarded	Master Degree in Cellular and Molecular Biology
Principal subject	Master Thesis Project: Structural characterisation of S-layer protein complexes from <i>Deinococcus radiodurans</i> R1
Skills covered	Biochemistry, Physical Chemistry, Structural Biology, Genetic, Molecular Biology, Microbiology, Physiology
Name and type of organisation providing education and training	University of Cagliari; Faculty of Biology and Pharmacy; Master Course in Molecular and Cellular Biology, Department of Life and Environmental Sciences; Laboratory of Structural and Molecular Plant Biology. Referent: Dr. Dario Piano
Level in national or international classification	Master of Science. 110/110 summa cum laude
<hr/>	
Dates	02/2014-03/2014
Principal subject	Internship: purification and characterization of enzymatic reactions performed by proteins which are validated target for drug development. Work Project: Identification of HIV-1 transcriptase (RT) associated ribonuclease H (RNase H) activity inhibitors and heterologous expression, purification and characterization of GEF protein from HIV
Name and type of organisation providing education and training	University of Cagliari (Italy); Department of Life and Environmental Sciences; Laboratory of Molecular Virology. Referents: Prof. Enzo Tramontano, Dr. Francesca Esposito
Level in national or international classification	Practical internship

---

Dates	15/01/2013 – 15/03/2013
Principal subject	Internship: purification, characterization and crystallization of membrane proteins. Work Project: Heterologous expression, purification and characterization of the Slow Anion Channel 1 (SLAC1) from Nanoarchaeum equitans
Name and type of organisation providing education and training	University of Regensburg (Germany); Institute of Biophysics and Physical Biochemistry. Department of Structural Biology. Referents: Prof. Christine Ziegler, Dr. Chitra Rajendran
Level in national or international classification	Practical internship founded by short-term individual fellowship for internship in European institution (grant)

---

Dates	20/10/2009 – 20/07/2012
Title of qualification awarded	Bachelor Degree in Biology
Principal subject	Bachelor Thesis Project: Deinococcus radiodurans R1: growth analysis under UV radiation in presence of different Manganese concentrations
Skills covered	Physics, Chemistry, Biochemistry, Genetic, Molecular Biology, Microbiology, Physiology
Name and type of organisation providing education and training	University of Cagliari; Faculty of Mathematics, Physics and Natural Sciences; Bachelor Course in Biology; Department of Life and Environmental Sciences; Laboratory of Structural and Molecular Plant Biology. Referent: Dr. Dario Piano
Level in national or international classification	Bachelor of Science. 110/110 summa cum laude

---

Dates	09/2004 – 07/2009
Title of qualification awarded	Diploma (High School)
Principal subjects covered	Italian and International Literature, Greek and Latin Language and Literature, Mathematics, Physics, Biology, Chemistry, Geology and Astronomy, English Language, Art, History, Philosophy.
Name and type of organisation providing education and training	(High School) Istituto “Liceo Ginnasio Statale G.Siotto Pintor”, Viale Trento 103/104 - 09123 Cagliari (Italy)
Level in national or international classification	90/100, Diploma (High School)

---

Dates	01/2007 – 05/2007
Title of qualification awarded	ECDL (European Computer Driving Licence)
Principal subjects covered	Basic concepts of Information Technology, Using the computer and managing files, Word processing, Spreadsheets, Database, Presentation, Information and communication
Name and type of organisation providing education and training	AICA - Italian Association for Informatics and Automatic Computation
Level in national or international classification	ECDL

### **Awards**

Date	2017 (award ceremony held on the 12 <sup>th</sup> of June 2017 at the University of Milan, Milan - Italy)
Title of qualification awarded	L'Oréal-UNESCO Research Fellowship for Women in Science (National recipient for Italy) - for accomplishments in scientific research. Project: “ <i>Functional and structural characterisation of the main S-layer protein DR_2577 of Deinococcus radiodurans</i> ”.
Name and type of organisation providing the award	L'Oréal Foundation and the United Nations Educational, Scientific and Cultural Organization (UNESCO)

---

Date 2015  
Title of qualification awarded Best graduate student award for 2015  
Name and type of organisation University of Cagliari, Cagliari (Italy)  
providing education and training

---

Dates 2009 – 2014  
Title of qualification awarded Individual annual scholarship for the best students of the year  
Name and type of organisation Autonomous Region of Sardinia (Italy)  
providing education and training

---

Dates 2009 – 2014  
Title of qualification awarded Individual annual scholarship for students  
Name and type of organisation ERSU (regional authority for the right to university studies)  
providing education and training

**Personal skills and competences**

Mother language Italian

Other language(s) English (C1), French (A2), German (A1)

## Publications

Gabriella Collu, **Domenica Farci**, Francesca Esposito, Francesca Pintus, Joanna Kirkpatrick, Dario Piano. *New insights into the operative network of FaEO, an enone oxidoreductase from Fragaria x ananassa Duch.* Plant Mol Biol, **2017**, doi:10.1007/s11103-017-0597-5.

**Domenica Farci**, Francesca Esposito, Sabah El Alaoui, Dario Piano. *S-layer proteins as a source of carotenoids: isolation of the protein cofactor deinoxanthin from its S-layer protein DR\_2577.* Food Res Intern, **2016**, doi: 10.1016/j.foodres.2016.10.003.

**Domenica Farci**, Joanna Kirkpatrick, Dario Piano. *A new procedure for a fast soft staining of BN-PAGEs on photosynthetic complexes.* Electrophoresis, **2016**, 38: 441-6. doi: 10.1002/elps.201600389.

**Domenica Farci**, Gabriella Collu, Joanna Kirkpatrick, Francesca Esposito, Dario Piano. *RhVII is a membrane-anchored vacuolar invertase highly expressed in Rosa hybrida L. petals.* J Exp Bot. **2016**, 67:3303-12. doi: 10.1093/jxb/erw148.

**Domenica Farci**, Chavdar Slavov, Enzo Tramontano, Dario Piano. *The S-layer protein DR\_2577 binds the carotenoid deinoxanthin and under desiccation conditions protect against UV-radiation in Deinococcus radiodurans.* Frontiers in Microbiology, section of Extreme Microbiology, research topic Photobiology of Extremophiles, **2016**, 7: 155, doi:10.3389/fmicb.2016.00155.

Patrycja Haniewicz, Davide Floris, **Domenica Farci**, Joanna Kirkpatrick, M. Cecilia Loi, Claudia Büchel, Matthias Bochtler, Dario Piano. *Isolation of plant Photosystem II complexes by fractional solubilisation.* Frontiers in Plant Sciences, Plant Cell Biology journal, research topic Assembly of the Photosystem II Membrane-Protein Complex of Oxygenic Photosynthesis, **2015**, 6:1100. doi: 10.3389/fpls.2015.01100.

**Domenica Farci**, Matthew W. Bowler, Francesca Esposito, Sean McSweeney, Enzo Tramontano, and Dario Piano. *Purification and characterization of DR\_2577 (SlpA) a major S-layer protein from Deinococcus radiodurans*. *Frontiers in Microbiology*, **2015**, *6*:414. doi:10.3389/fmicb.2015.00414

**Domenica Farci**, Matthew W. Bowler, Joanna Kirkpatrick, Sean McSweeney, Enzo Tramontano and Dario Piano. *New features of the cell wall of the radio-resistant bacterium Deinococcus radiodurans*. *Biochim Biophys Acta*, **2014**, *1838*: 1978-84. doi:10.1016/j.bbamem.2014.02.014.

**Posters presentations** **Domenica Farci**, Chavdar Slavov, Matthew W. Bowler, Dario Piano. (September 2016). *The S-layer as a UV-radiation shield: the case of Deinococcus radiodurans and its S-layer Deinoxanthin Binding Complex*. **Joint Congress of the French and Italian Photochemists and Photobiologists, Università Aldo Moro, Bari, Italy.**

**Domenica Farci**, Chavdar Slavov, Matthew W. Bowler, Dario Piano. (May 2016). *The S-layer as a UV-radiation shield: the case of Deinococcus radiodurans and its S-layer Deinoxanthin Binding Complex*. **Gordon Research Conference – Carotenoid Biosynthesis, Functions, and Application to Human Health, Pisa, Italy.**

Patrycja Haniewicz, Davide Floris, **Domenica Farci**, Joanna Kirkpatrick, M. Cecilia Loi, Claudia Büchel, Matthias Bochtler, Dario Piano. (September 2015). *A facilitated isolation of PSII cores and PSII-LHCII supercomplexes by a selective solubilisation of the thylakoid membranes*. **Joint Congress SIBV-SIGA, Milano, Italy.**

**Domenica Farci**, Monika Gunkel, Ashraf Al-Amoudi, Stephan Irsen, U. Benjamin Kaupp. (October 2015). *Insight into the sea urchin sperm flagellum: the highly ordered guanylate cyclase*. **5<sup>th</sup> International caesar conference, Bonn, Germany.**

**Domenica Farci**, Monika Gunkel, Ashraf Al-Amoudi, Stephan Irsen, U. Benjamin Kaupp. (September 2015). *Insight into the sea urchin sperm flagellum: the highly ordered guanylate cyclase*. **EMBO course Cryo-EM 2015, London, United Kingdom.**

Pierluigi Cortis, **Domenica Farci**, Maria Cecilia Loi, Dario Piano.  
(September 2013). *Structural and functional analysis of Photosystem II from Nicotiana tabacum L.* **108° Congress SBI Onlus, Trento, Italy.**

**Oral presentations** **Domenica Farci**, Chavdar Slavov, Matthew W. Bowler, Dario Piano.  
(September 2016). The S-layer as a UV-radiation shield: the case of *Deinococcus radiodurans* and its S-layer Deinoxanthin Binding Complex.  
**Joint Congress of the French and Italian Photochemists and Photobiologists, Università Aldo Moro, Bari, Italy.**

**Conference participation** *Cryo-EM Symposium, European Photon & Neutron Campus, Grenoble, France. 6-7 July 2017.*

*Joint Congress of the French and Italian Photochemists and Photobiologists, Università Aldo Moro, Bari, Italy. 19-22 September 2016.*

*Ligands Recognition and Molecular Gating, Gordon Research Conference, Renaissance Tuscany Il Ciocco, Lucca (Barga), Italy. 31 January – 5 February 2016.*

*Insight into the sea urchin sperm flagellum: the highly ordered guanylate cyclase, 5<sup>th</sup> International caesar conference, Bonn, Germany – 30 September – 2 October 2015.*